NUMERICAL ANALYSIS OF A PV/MICROCHANNEL INTEGRATED

CO_2 DIRECT-EXPANSION HEAT PUMP WATER HEATER

A Thesis
Submitted to the Graduate Faculty
of the
North Dakota State University
of Agriculture and Applied Science

By

Mohammad Rajib Uddin Rony

In Partial Fulfillment of the Requirements
for the Degree of
MASTER OF SCIENCE

Major Department:
Mechanical Engineering

June 2019

Fargo, North Dakota

North Dakota State University
Graduate School

Title

NUMERICAL ANALYSIS OF A PV/MICROCHANNEL INTEGRATED
CO_2 DIRECT-EXPANSION HEAT PUMP WATER HEATER

By

Mohammad Rajib Uddin Rony

The Supervisory Committee certifies that this ***disquisition*** complies with North Dakota

State University's regulations and meets the accepted standards for the degree of

MASTER OF SCIENCE

SUPERVISORY COMMITTEE:

Dr. Adam Gladen

Chair

Dr. Jordi Estevadeordal

Dr. Yan Zhang

Dr. Huojun Yang

Approved:

July 29, 2019   Dr. Alan Kallmeyer

Date   Department Chair

ABSTRACT

A steady-state numerical model of a PV/microchannel integrated direct-expansion CO_2 heat pump (PV-DXHP) water heater is developed, validated, and analyzed in the present study. To accomplish the objectives, a numerical model of a microchannel evaporator integrated into a CO_2 PV-DXHP is developed and validated. The effects of evaporator operating parameters on the heat absorption and pressure drop are analyzed. Utilizing the evaporator model, the PV-DXHP model is developed, and the baseline values of the heat pump operating parameters are determined from the evaporator parametric study. The PV-DXHP demonstrates high water heating capability while maintaining a reasonably high COP. The COP has the highest dependency on the CO_2 mass flow rate, while the water outlet temperature has the highest dependency on the water mass flow rate. The results are highly promising and indicate the system has potential to help meet the energy requirements for residential and industrial water heating demands.

ACKNOWLEDGEMENTS

TABLE OF CONTENTS

LIST OF TABLES

LIST OF FIGURES

LIST OF ABBREVIATIONS

HP………………………………….. Heat Pump

CFC…………………………………Chlorofluorocarbons

HFC…………………………………Hydrofluorocarbons

GWP………………………………...Global warming potential

COP…………………………………Coefficient of performance

ODP…………………………………Ozone depletion potential

IHX…………………………………Internal heat exchanger

HX…………………………………..Heat exchanger

HTC…………………………………Heat transfer coefficient

DSH…………………………………Degree of superheat

MCHX………………………………Microchannel heat exchanger

FGB…………………………………Flash gas bypass

CDP…………………………………Compressor discharge pressure

HEM……………………………….. Homogeneous equilibrium model

EEV…………………………………Electronic expansion valve

ASHP………………………………. Air source heat pump

ESC………………………………… Extremum seeking control

WSHP………………………………Water source heat pump

GSHP……………………………… Ground source heat pump

GCHP………………………………Ground coupled heat pump

nZEB………………………………..Net zero energy balanced

GSAHP……………………………...Geothermal-solar assisted heat pump

HPWH………………………………Heat pump water heater

LIST OF SYMBOLS

A..area (m^2)

Bo..boiling number

C..Chisholm parameter

C_p..specific heat (J·kg^{-1}·K^{-1})

D..diameter (m)

E..output electricity (W)

f..friction factor

F..Reynolds number factor

h..enthalpy (J·kg^{-1})

I..solar irradiance (W·m^{-2})

G..mass flux (kg·m^{-2}·s^{-1})

Nu..Nusselt number

p..pressure (Pa)

Pr..Prandlt number

q..heat flux

Q..heat gain (W)

r..reflectivity

R..thermal resistance (K·W^{-1})

Re..Reynolds number

s..slip ratio

S..suppression factor

T..temperature (K)

v..specific volume

W..Work done

Greek Letters

α..heat transfer coefficient (W·m^{-2} ·K^{-1})

β..absorptivity

ε………………………………………..emissivity

η…………………………………………..efficiency

κ…………………………………………..temperature coefficient (K^{-1})

ω…………………………………………Void fraction

φ^2……………………………………...two-phase multiplier

Φ…………………………………… sensitivity coefficient

σ……………………………………….S-B constant ($W{\cdot}m^{-2}{\cdot}K^{-4}$)

δ………………………………………. thickness of the copper plate

μ……………………………………. dynamic viscosity (Pa·s)

ρ………………………………………..density ($kg{\cdot}m^{-3}$)

$\tau\beta$…………………………………… effective absorptivity

Subscripts

a………………………………………..air; ambient

a-e………………………………….. between ambient and evaporator

b………………………………………..bulk

b-pv…………………………………… between copper plate and PV panel

c…………………………………………..compressor

$conv$…………………………………… convective

d…………………………………………..displacement

di…………………………………… dryout

e………………………………………..evaporator

f……………………………………….. liquid

g…………………………………………..vapor; glass

i……………………………………….. inner, inlet

o………………………………………..outer

p………………………………………..pipe

w……………………………………….water

LIST OF APPENDIX FIGURES

1. INTRODUCTION

1.1. General Introduction

Residential solar energy systems in the United States has become more accessible and prevalent than ever before [1]. Conventionally, solar thermal collectors are used to meet hot water demand, while PV panels are used to generate electricity. In recent years, the combination of the two technologies known as photovoltaic–thermal (PV-T) system has gained momentum, since it can produce both hot water and electricity along with ensuring efficient use of valuable roof space. Moreover, the cost of PV panel installation has dropped over 70%, making the PV-T system more cost-effective [2].

Among different configurations of PV-T systems, a PV-DXHP is well suited for residential solar thermal applications [3, 4]. In a PV-DXHP, the refrigerant absorbs waste heat directly from the PV panels and evaporates, eliminating the need for a secondary heat exchanger. Experimental studies have confirmed that the yearly average coefficient of performance (COP) of a PV-DXHP is superior to a conventional heat pump system [5, 6]. Further, Huang et al.'s [7] experiments have affirmed that PV-DXHP can be employed in regions with low ambient temperatures.

A key aspect of a PV-DXHP is the evaporator configuration. Various designs such as flat plate, multi-pass, double-tube and tube-and-fin have been investigated [8–10]. However, these traditional designs have issues such as susceptibility to leakage and deformation. To overcome such issues, studies have shown that a microchannel HX is a promising alternative because it has several advantages over conventional HXs. For instance, the microchannel structure can endure high working pressure as well as facilitate high refrigerant vapor flow velocity and a larger contact area per unit fluid volume, yielding a higher heat transfer coefficient [11, 12]. Rin Yun et al. [13] carried out a comparative study between a microchannel HX and the conventional fin-tube HX for

two different working fluids (R134a and CO_2). The test results have indicated that irrespective of the working fluids the microchannel has shown to aid higher heat transfer rates.

A PV integrated microchannel-evaporator DXHP with R410a as the refrigerant was experimentally investigated by Zhou et al. [14]. Under real-time operational conditions, the system could achieve an overall system efficiency of 69.7%. The designed, parallel-laid microchannel ensured increased vapor flow velocity within the channel resulting in high shear stress leading to reduced liquid film thickness and increased refrigerant evaporation rate. The test results have shown that with R410a as the refrigerant the system could provide hot water in the range of 30 - 40 °C. However, water must be stored at > 50 °C to avoid harmful bacteria growth [15], thus this system would require a supplemental heating source.

It is hypothesized that water temperatures >50 °C can be attained by using CO_2 as the refrigerant since its thermo-physical properties are particularly conducive for heating applications [16]. Moreover, the natural refrigerant CO_2 does not have the environmental concern as of the CFCs and (H)CFCs [17].

To the author's knowledge, there exist no numerical studies on PV/microchannel evaporator integrated DXHP system using CO_2 as the working fluid. As such, the present work develops an in-depth numerical model and validates it with experimental data in order to predict the performance of such a system. The effects of operating parameters on the system performance are investigated. A sensitivity analysis is performed to analyze the relative significance of the operating parameters on the system performance parameters. In addition, a seasonal performance analysis is carried out to predict the system seasonal performance in Fargo, North Dakota weather conditions.

2

1.2. System Description

Figure 1.1 shows the schematic of the PV/microchannel evaporator integrated CO_2 DXHP water heating system. The system consists of four major components: PV/microchannel evaporator module, which is a combination of PV panels and microchannel heat exchangers; a variable speed compressor; a gas cooler, which is a counter-flow tube-in-tube heat exchanger transferring heat from the refrigerant to the water; and an expansion device. The system would also have supplementary components such as a PV controller, an inverter, and batteries for smooth and stable operation of the heat pump system. However, the current work does not model these supplementary components.
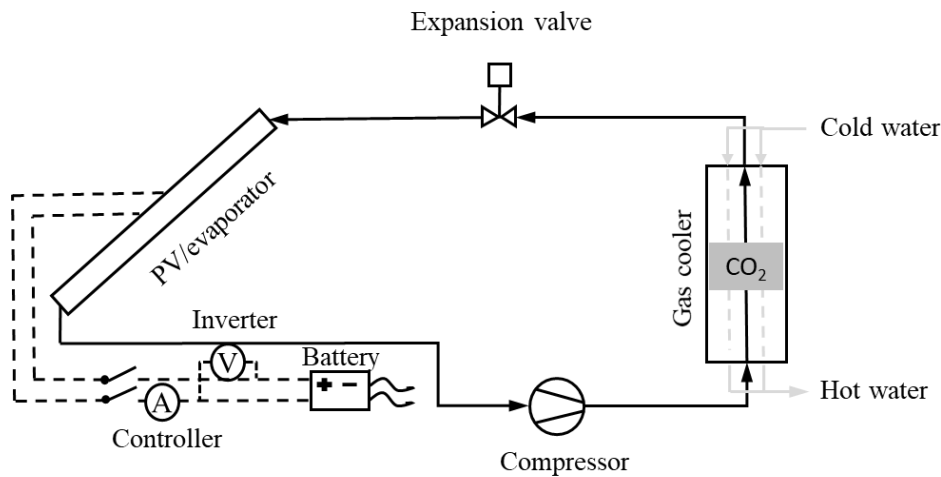
Figure 1.1: Schematic diagram of the Heat Pump System.

Figure 1.2 presents a simplified idealized version of the pressure-enthalpy diagram of the CO_2 transcritical cycle. Initially, CO_2 flows through the microchannel evaporator integrated at the bottom of the PV panels. In the evaporator, the refrigerant absorbs part of the waste heat from the PV panels. The CO2 enters as a two-phase fluid and exits the evaporator as a superheated vapor (1 – 2). The evaporated refrigerant is directed into the compressor where it is pressurized to a supercritical vapor pressure state (2 – 3). The supercritical CO_2 heats the domestic water supply in

3

the gas cooler and exits as a supercritical fluid but at a lower temperature $(3-4)$. Finally, the high pressure but low-temperature CO_2 is throttled through the expansion valve $(4-1)$ to the evaporator pressure.
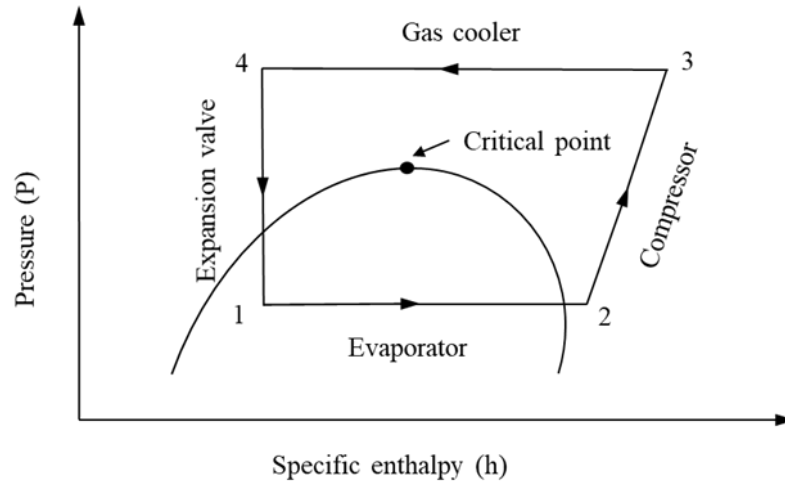
Figure 1.2: P-h diagram of transcritical CO_2 heat pump cycle.

1.3. Thesis Outline

The thesis is detailed in nine chapters. A literature review of various technologies or approaches applied and tested on CO_2 HPs is presented in chapter 2. The objectives of the thesis are summarized in chapter 3. In chapter 4, the evaporator model is described, and key operating parameters are analyzed to find the optimum conditions for heat absorption and pressure drop. The detail mathematical model of the heat pump system is presented in Chapter 5. In Chapter 6, the numerical simulation procedure is described, and the mathematical model is validated. The scope of the study is presented in chapter 7. In chapter 8, the heat pump operating parameters are analyzed, and a sensitivity analysis of the operating parameter is presented. Chapter 9 summarizes the important findings from the study and suggests future research direction.

2. LITERATURE REVIEW

The objective of this review is to analyze various technologies or approaches applied and tested on CO_2 HPs. A brief overview of CO_2 heat pump applications and a comparison between conventional HP cycles with the transcritical cycles is provided to understand the applicability of CO_2 in HP applications. The supercritical and two-phase heat transfer characteristics of CO_2 in different heat exchanger (HX) configurations are briefly analyzed. Furthermore, recent modifications of each HP component and their impact on heating applications concerning different heat sources are detailed and discussed. The following literature review is a condensed version of the literature review written by this thesis author and published in Energies [17].

2.1. CO$_2$ Heat Pump Applications

CO_2 HPs are environmentally-friendly and energy-efficient, which makes them popular for various applications such as hot water production, space heating, and dehumidifying (drying). In this section, a comprehensive overview of recent advances in CO_2 heat pump based on applications is presented.

2.1.1. Water Heating

Water heating accounts for roughly one-fifth of the energy consumption in a typical residential building in the USA [17]. Hence, water heating is the main purpose of a transcritical CO_2 HP for providing both service hot water and space heating. Based on the heat transfer performance of each component in a transcritical CO_2 HP water heater, Yamaguchi et al. [18] carried out a numerical simulation and found that the maximum attainable COP was 3.6. The study concluded that the CO_2 HP water heater instead of an electric or gas water heater can lead to a significant reduction in primary energy consumption. In addition, a CO_2 HP water heater (HPWH) prototype [19] was developed at Oak Ridge National Laboratory (ORNL), which meets ENERGY

STAR standards [20] for HPWHs at a low cost. The main design feature is that the prototype uses an optimized wrap-around gas cooler (roll flexible HX) instead of an external HX. ORNL estimated that the CO_2 HPWH can reduce energy use by 0.8 quads a year, whereas the annual energy consumed by electric water heaters are approximately 1.38 quads.

Saikawa et al. [21] carried out a thermodynamic analysis of an HP using the fluorocarbons and natural refrigerants. The theoretical study illustrated that, among all the refrigerants tested, the transcritical CO_2 HP had the highest COP and the theoretical limit was 6.0 from a technical viewpoint. They developed a prototype for residential hot water production, which could attain a COP of 3.0, and emphasized on energy recovery in the expansion process, and the efficiency improvement of the compressor and HXs to further improve the prototype's COP.

2.1.2. Dehumidification (Drying)

In a CO_2 HP, the cooling capacity can be utilized to dehumidify the moistened air, while the heating capacity heats the cold air. Klocker et al. [22] experimentally studied a CO_2 HP dryer and compared its performance with a conventional electric resistance dryer. The results showed that the CO_2 HP dryer could reach a temperature of about 60 °C whereas the typical electric resistance dryer could reach up to 130 °C. One advantage of reaching a low temperature is that the temperature sensitive merchandises' safety can be preserved. Moreover, for the compressor with a larger heat capacity, the drying time was shorter, and the system COP was higher due to the lower discharge pressure of the compressor. This HP dryer was found to be 65% more energy-efficient as compared to an electric resistance dryer. Schmidt et al. [23] thermodynamically compared a transcritical CO_2 dehumidification cycle with a subcritical R134a cycle for drying purposes and found that the two cycles could be energetically equivalent if a better isentropic

efficiency of compression can be achieved in the CO_2 cycle. Henceforth, the CO_2 is the effective candidate for its environmental concern.

2.1.3. Cold Climate Heating

HPs' heating performance diminishes as the ambient temperature decreases, and specific modifications are required for energy efficient performance in cold climates. The air source heat pump (ASHP) loses efficiency in a low outdoor temperature due to frost formation on the evaporator coil, while GSHP COP reduces in cold climates due to a soil thermal imbalance in long-term operation. The HP compressor suffers premature wear and tear in cold climates due to load imbalance at a low ambient temperature. Moreover, the required high initial cost limits the use of HPs in cold climates.

However, many studies have contributed to enhancing HP performance in a cold climate. Wang et al. [24] experimentally studied a transcritical CO_2 HP for cold climate operation and found that the HP could achieve a COP of 3.1 at the outdoor temperature of -20 °C. However, integration of a secondary loop cycle in the system increased the gas cooler outlet temperature and reduced the COP by 19% compared to a CO_2 HP without a secondary loop. Hakkaki-Fard et al. [25] found that the 80/20 R32- CO_2 zeotropic mixture could enhance the heating performance of an ASHP in cold climates by 30% compared to an R410a system. The zeotropic mixture could also reduce the flammability of R32 and the CO_2 pressure in the operation. They reported R32 - CO_2 mixture is the best-suited refrigerant mixture for the cold climate among all the mixtures tested. In another study, Hakkaki-Fard et al. [26] found a variable mixture of the R32-CO_2 refrigerant, which could save up to 23% energy in a cold climate while reducing GWP by 16%. Other than research studies, several split type systems are commercially available and designed to provide smooth operation in severe climate conditions. The split-system components

are robust and can operate in any given climate. Such a CO_2 split HP can lead to an efficiency of up to 400% [17], and it also can generate hot water up to 80 °C whereas its effective operating temperature at the evaporator can be as low as –30 °C. Although there are several commercial split-systems available in the Asian and European markets (e.g., Sanyo [27]), only the Sanden's SAN CO_2 split-system HPWH [28] is available in North America. Mitsubishi is also developing such a CO_2 HP system for residential applications [17].

2.2. Comparison of Transcritical and Conventional Heat Pump Cycles

The transcritical HP cycle is thermodynamically different than a conventional, sub-critical vapor-compression HP or refrigeration cycle. As shown by the pressure-enthalpy diagram of Figure 2.1, both cycles have the same four main processes: heat rejection, expansion, evaporation (heat addition), and compression. The primary difference is in the heat rejection process (Figure 2.1). During the heat rejection process of a sub-critical cycle, the refrigerant changes its phase at a constant temperature whereas, in the transcritical cycles, the refrigerant temperature decreases continuously throughout the heat rejection process without a phase change. Although latent heat exchange is an efficient heat transfer path, the supercritical properties of CO_2 make it a viable candidate for transcritical HP systems. When the CO_2 vapor is compressed beyond the critical point (31.1 °C, 7.38 MPa), it can deliver much higher heat rejection enthalpy through sensible cooling [17].

However, in a CO_2 transcritical cycle, the pressure difference between heat absorption and heat rejection is much higher than a typical subcritical cycle, which results in significant thermodynamic losses in the expansion process. The large pressure difference makes it feasible to use expansion work recovery devices in a transcritical cycle, which can partially compensate for the throttling losses in the transcritical CO_2 cycle [29]. While the pressure difference is higher than

8

traditional refrigerants, the pressure ratio is lower. For example, the conventional subcritical cycle with R134a operates at a pressure ratio up to eight, whereas the CO_2 transcritical cycle operates at a pressure ratio within the range of three to four [17]. Such low compression ratios are conducive for achieving high isentropic efficiency in an HP system. In both cycles, the evaporation (heat absorption) process occurs below the critical temperature, and, hence, the pressure remains subcritical.

| (**a**) | (**b**) |
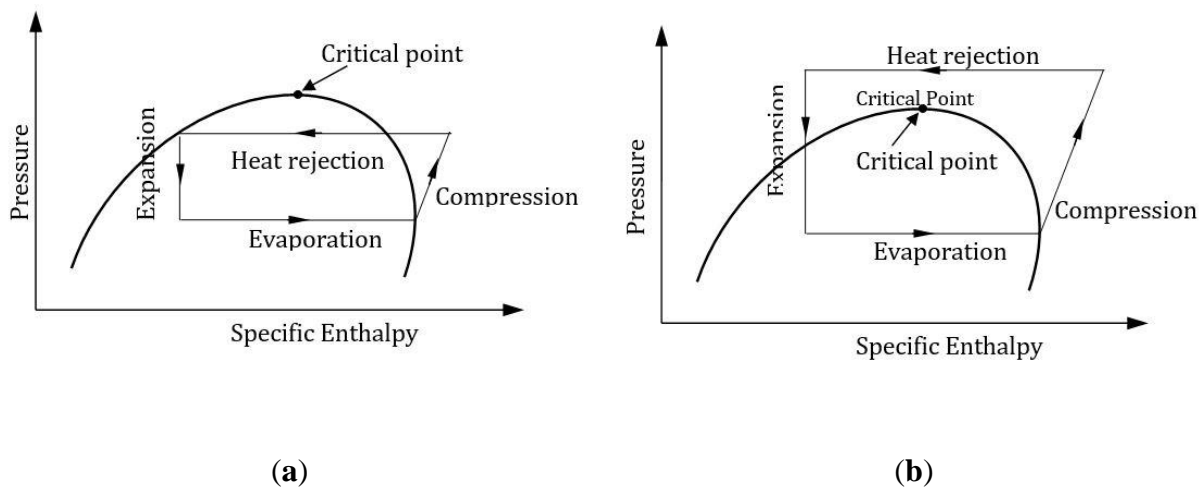
Figure 2.1: P–h diagrams: (**a**) Subcritical cycle and (**b**) Transcritical cycle [30].

2.3. CO_2 Heat Pump Systems

According to the available heat sources at the evaporator side, HPs can be classified by heat source: air source, water source, or ground source HP. A hybrid HP is defined as an HP using more than one heat source. In hybrid systems, most commonly solar and geothermal energy are incorporated with the conventional heat sources to improve the system performance. In the following subsections, each type of system is discussed and detailed.

2.3.1. Single Heat Source Systems

In air source heat pump (ASHP), the low temperature refrigerant absorbs heat from air to evaporate. It has been in use in the USA for many years but not in the regions where the ambient

temperature gets below the freezing point during the winter due to frosting in the evaporator. However, recent technology advances make ASHP viable in cold climate regions. Hu et al. [31] experimentally studied a transcritical CO_2 driven ASHP for water heating in a cold climate in which a hot gas bypass defrosting method was utilized to overcome the frosting at low ambient temperatures. The energy analysis showed that the gas cooler consumed 57.4% of the supplied energy to increase the internal energy, while 35% for the frost melting process, which is typically higher than other defrosting methods. The experimental results showed that the hot gas bypass defrosting method could only achieve efficiency as high as 40%. Calabrese et al. [32] conducted an experimental study on a transcritical CO_2 ASHP installed on a building rooftop in which the inlet air at the gas cooler was a combination of fresh air supplied from the environment and recirculated air from the HP system. The rooftop HP COP was found to be 2.8 when the gas cooler inlet air temperature was 6 °C, which is lower than typical heat pump working with HFCs. In order to enhance COP of ASHP, Hu et al. [33] proposed an extreme seeking control (ESC) method to optimize the system COP. Their simulation results indicated that the ESC could find and slowly adopt the inputs (discharge pressure) to maintain the COP at an optimum level for water outlet temperature from 55 to 80 °C without the need for a system upgrade. The heat pump optimum COP was 3.29, while heating water to 60 °C. Most recently, Hu et al. [34] developed another control system based on ESC to optimize the power consumption to maximize COP.

In water source heat pump, a water source such as lake is used from which the low temperature refrigerant absorbs heat to evaporate. Such type of heat pump is best suited where simultaneous heating and cooling is required. The operation of WSHP is much quieter along with a low carbon footprint compared to ASHP. In moderate climate conditions, WSHP can be used since the heat rejected at the cooling unit can be utilized to maintain a certain temperature at the

heating unit. However, in a cold climate, the major problem associated with WSHP is the water freezing in the evaporator. For a dual mode CO_2 WSHP, Liu et al. [35] experimental demonstrated an optimal, overall COP of approximately 5.0 by using a variable frequency compressor which allowed for better thermal stratification in the tank. Murray et al. [36] found in their study that CO_2 WSHP can achieve an average COP of 3.1 for corresponding average water temperature of 70 °C. Recently, Mayekawa Company from Australia [17] developed a commercial CO_2 WSHP.

In ground source heat pump (GSHP) pump, the CO_2 flows through a bore hole (horizontal or vertical) and uses the thermal energy in the ground to evaporate. Due to the drilling requirements, installing GSHP is more expensive than other HP systems. However, GSHPs highlight the potential of CO_2 over other refrigerants. GSHPs with conventional refrigerants can only provide hot water up to 60 °C, whereas a CO_2 GSHPs can supply water of 90 °C or even higher [17]. Wang et al. [37] modeled a CO_2 GSHP cycle with a U-tube ground HX and found that it could achieve an equivalent performance as that of the conventional R134a and R22 HP cycles. Moreover, use of an expander yielded the COPs of 5.5 and 5.9 in the summer and the winter, respectively, which were higher than a baseline CO_2 GSHP system without the expander.

Nejad et al. [38] modeled a steady-state two-phase CO_2 filled vertical borehole that could be used as a direct-expansion evaporator for a GSHP during the heating mode. The study analyzed the thermal performance of the borehole along with the effect of pressure, temperature, and quality of CO_2 on the performance, and compared the results with a single-phase borehole system. The simulation results indicated that the two-phase heat transfer coefficient of CO_2 is exceptionally conducive for greater heat extraction from the borehole. This is due to, at a relatively small variation in CO_2 temperature (0 °C to −1.8 °C), a large amount of energy is available because of

11

the large latent heat of vaporization. However, the temperature variation in the single-phase region was significantly high (maximum of 6.3 °C), which leads to a relatively low heat extraction.

2.3.2. Hybrid Heat Pump Systems

Interest in hybrid systems has grown over time due to the necessity of employing sustainable renewable energy sources. To meet the energy demand for residential and commercial heating/cooling as well as hot water demand, researchers have not only developed novel hybrid systems but also suggested improvements for the existing system configurations.

2.3.2.1. *Hybrid Solar/PV-T Systems*

Use of low-grade heat sources such as solar energy as an auxiliary energy source integrated with a heat pump to obtain net zero energy balanced (nZEB) has been considered and explored by many researchers. A solar-assisted CO_2 HP is typically more energy efficient than baseline HPs due to reduced electricity consumption [17]. Deng et al. [39] found that a hybrid solar-assisted heat pump integrated with a solar-thermal driven absorption chiller can reduce the electricity consumption by 13.7% compared to a baseline CO_2 heat pump and achieve a COP of 2.64. In a similar study, Deng et al. [40] carried out a comparative study of an hybrid air-cooled, solar assisted CO_2 HP and an ideal, air-cooled CO_2 HP. The hybrid HP integrated a conventional CO_2 HP. Simulation results showed that the cooling performance could improve with an increased super-cooling temperature difference. The cooling COP reached 3.8 at the super-cooling temperature difference of 7.7 °C. Additionally, the hybrid system was found to reduce the power consumption by ~19% compared to a conventional CO_2 HP without the absorption chiller. Further experimental work showed that using such a hybrid system, 58% of the total energy consumed per year could meet the energy demand for HVAC and domestic hot water (DHW) in nZEB apartments. Additionally, a solar-assisted ground source heat pump was simulated by Emmi et al.

[41] for cold climates, and it showed that the integration of solar energy helped to recharge the ground in the long run, and thus increased the HP efficiency by 30%.

Chen et al. [42] formulated a numerical model to analyze the effects components on the performance of a solar-assisted CO_2 HP, while a multi-parameter optimization was performed to minimize the electrical consumption and considering the influence of storage and operation tanks. They found that the HP could attain a higher COP and reduce electricity consumption compared to a baseline CO_2 HP when heating water to 50 °C. Faria et al. [43] developed a dynamic mathematical model to investigate a CO_2 HP integrated with a flat plate collector (solar evaporator) and expansion valve assembly under both the steady state and transient conditions. They reported that adjusting the expansion valve opening had a noticeable effect on the system's performance. If the CO_2 is heated to a high degree of superheating, the HP's performance drastically decreased because the DSH reduced the boiling (two-phase) region, which consequently increased the dry (gas only) area. This resulted in a low convective coefficient value. They recommended that, for a CO_2 driven HP with a solar evaporator, the use of an EEV is essential to continuously adjust the CO_2 flow to the evaporator in order to maximize the system's performance. Unlike Faria et al.'s design [43], a U-pipe, evacuated-tube solar collector with low-levels of concentration was utilized as the evaporator in Islam et al.'s work [44]. Islam et al. showed that the system COP could be improved by an average of 57% with a compressor speed decrease from 1500 to 900 rpm. They found that the collector efficiency was in the range of 50% to 55%. Though the initial cost of the U-pipe solar collector HP systems is relatively higher when compared to the non-focusing collectors, the system can be a better prospect in the future for thermal applications since such a system is environmentally benign.

Given that the thermophysical properties of a refrigerant play an important role in dictating the HP performance, CO_2 has been compared with other conventional refrigerants in hybrid solar HPs. Li et al. [45] presented a simulation on a hybrid, solar-assisted HP using R134a, CO_2 (R744), and R22 for water heating in a residential apartment. The results showed that for ambient temperature ranged from -5 to 13 °C, the CO_2 attained a higher COP compared to R134a and R22. However, R134a attained the maximum COP when the ambient temperature was above 13 °C, while CO_2 HP attained a low cooling efficiency under all operating conditions. Cho et al. [46] presented a similar study on a solar assisted HP system using CO_2 and R22 and found that, during sunny days, COPs for both CO_2 and R22 were 20% higher compared to cloudy days. However, concerning the second law efficiency, the R22 system had a 6.2% higher efficiency compared to the CO_2 due to the higher irreversibility.

2.3.2.2. Hybrid Geothermal

To further improve the performance of CO_2 HP and increase the energy saving potential, hybrid geothermal HP systems with a secondary heat source/sink such as solar energy, ambient air, or water has been studied. Jin et al. [47] theoretically analyzed a hybrid Geothermal HP system, which utilized a combination of ambient air and ground boreholes as the heat sink for cooling mode. The boreholes were only engaged as the heating source during the heating mode. The system used two separate gas coolers known as the air-cooled gas cooler and the water-cooled gas cooler for the heat rejection process to take advantage of the large temperature glide. The results showed that depending on the indoor temperature, the time-dependent COP_{cool} varied from 2.2 to 4.1, while the COP_{heat} varied from 2.53 to 3.15. Jin et al. [48] further extended this study using a reverse CO_2 transcritical cycle for a CO_2 hybrid geothermal HP system. The system was able to operate under space cooling or heating mode with a simultaneous water heating. The results showed that the

14

combined COP for space conditioning and hot water varied from 3.0 to 5.5 with 65 °C of the service hot water supply.

During the last decade, the hybrid geothermal-solar assisted HPs (GSAHPs) have gained researchers' attention, potentially for both space heating and hot water supply. Emmi et al. [41] simulated a GSAHP and evaluated its performance in cold climates where the heating and cooling load profiles of buildings were not balanced. The integration of solar collector with the HP was found to enhance the efficiency by 30% with the COP ranging from 3.59 to 4.70 for different seasonal conditions. Kim et al. [49] investigated the performance of a CO_2 hybrid GSAHP under different operating conditions. The results showed that changing the operating temperature from 40 to 48 °C resulted in about a 20% increase in the compressor pressure ratio, which caused an increase of the compressor power consumption from 4.5 to 5.3 kW. Additionally, with the rise in daily solar radiation from 1.0 to 20 MJ/m^2, the heat in the collector increased by around 50%. They suggested to consider the operational characteristics and design parameters while designing a CO_2 GSAHP to increase system reliability and reduce energy consumption.

2.4. CO_2 Heat Pump Component Modifications

The performance of a CO_2 heat pump depends on the interaction between all components. However, individual component design and performance has an impact on the overall performance. Research has been done to improve the design of the components and in this section, recent studies pertaining to CO_2 heat pump components improvement are discussed.

2.4.1. Evaporator

The CO_2 HP evaporator functions like conventional CFC or HFC HP evaporators except that it experiences a much higher pressure (2–7 MPa) in the subcritical region. The CO_2 evaporator operates at a reduced pressure higher than 0.36, at a saturation temperature of

approximately -10 °C whereas an R134a evaporator works at a reduced pressure below 0.10, at a saturation temperature of 10 °C [50]. Consequently, the transport properties of CO_2 in the subcritical region (e.g., high vapor density and low vapor viscosity) are substantially different from the other refrigerants. The CO_2 flow in the evaporator is characterized by two-phase flow, and the transport properties drastically influence the nucleate boiling, the convective heat transfer, and the CO_2 pressure drop. Recent numerical and experimental studies focus on improving the efficiency of CO_2 evaporator by considering the flow characteristics. To ensure the feasibility of a CO_2 HP, it is essential to design the evaporator as a compact, lightweight, and reliable system [51].

A main consideration of the evaporator design is the size of the tubing through which the CO_2 flows. Evaporators consisting of microchannels or minichannels for the CO_2, rather than macrochannels, have been investigated due to enhanced HTC, minimized leakage, and reduced refrigerant charge possible with mirco- or minichannels. Microchannel is defined as the diameter < 3mm, and macrochannel is defined as diameter > 3mm [52]. Carbon dioxide is a good candidate to take advantage of micro- or minichannels. Choi et al. [53] investigated CO_2 two-phase heat transfer in horizontal mini-channels and reported that CO_2 HTC increases with an increase in vapor quality. Moreover, CO_2 HTC was found to be three times higher than R143a. Based on their experimental study, they proposed a separate two-phase flow heat transfer model for CO_2 flowing in smooth mini-channels. Oh et al. [54] experimentally studied five different refrigerants in mini-channels and found that CO_2 has the highest boiling HTC. Wu et al. [55] and Yun et al. [56] further reported that the nucleate boiling is predominant at a lower vapor quality because the heat flux and saturation temperature dictate the local HTC in this region, while the convective HTC dominates due to a high vapor velocity at a higher vapor quality. Wu et al. [55] evaluated the pressure drop

across the mini-channel by modifying the frictional factor developed by Cheng et al. [57] to address the overprediction of a frictional pressure drop in the mist flow region.

Concerning the evaporator configuration, several types of CO_2 HXs, such as microchannel, flat plate, multi-pass, double-tube, and tube-and-fin have been studied. In a study of an electric vehicle HP system in a cold climate, Wang et al. [24] found that the micro-channel evaporator had less than 4% exergy loss in all operating conditions. Yun et al. [58] simulated a three-slabbed micro-channel evaporator using R134a and CO_2 as the working fluid and compared their performance. The numerical results showed that the overall system performance could be enhanced by increasing the two-phase flow region in the micro-channel. There was a 70% increase in the two-phase flow region when the fin spacing was manipulated from 1.5 to 2.0 mm, and such a marginal increase in the spacing not only reduced material cost but also helped to eradicate the defrosting and condensation drainage problem. Furthermore, the selection of an appropriate circuiting arrangement is found to be imperative to ensure a higher heat transfer in a CO_2 evaporator. Bendaoud et al. [59] developed a new model accounting for the thermal and hydrodynamic behavior of a fin and tube HX. The developed tool was used to study a typical CO_2 evaporator coil consisting of two circuits in a parallel counter-current configuration. The study showed that the pressure drop was very low for CO_2 compared to other refrigerants, and, as a result, the temperature glide was limited considerably. In another study, Yamaguchi et al. [18] experimentally and numerically studied a cross-fin tube HX with smooth plate fins as a CO_2 evaporator for the water heating application, and the results confirmed that the heat exchange rate in the evaporator decreased (20 to 12 kW) with a rise in inlet water temperature (8 to 44 °C). Yun et al. [58] compared a two-slabbed micro-channel evaporator and a conventional round fin-tube HX for a CO_2 system, and they found that the micro-channel evaporator aided a 33% increase in

performance compared to the round fin tube HX. This was attributed to the larger effective surface area, especially with a V-shaped micro-channel HX (MCHX) yielding a higher HTC.

The CO_2 two-phase heat transfer in macrochannels and microchannels depends on the refrigerant mass flux, heat flux, channel geometry, and saturation temperature [50]. In an investigation of CO_2 two-phase heat transfer and pressure characteristics in a conventional macro-channel, Yoon et al. [60] reported that CO_2 boiling HTC increased with the increase in heat flux at the low vapor quality but decreased with the increase in heat flux when the vapor quality was above a specific value. This can be explained by the inception of vapor dryout at a high vapor quality due to an increase in heat flux, low surface tension, and reduced viscosity. The pressure drop was found to increase with an increase in mass flux, while there was an opposite trend for increasing the saturation temperature. Bredesen et al. [61] and Knudsen et al. [62] found in their experimental studies that the two-phase heat transfer in large tubes could be enhanced significantly by increasing the heat flux without a considerable pressure drop.

Based on the discussion, the microchannel evaporator configuration using CO_2 as the refrigerant certainly has the advantages of high heat transfer coefficient, less susceptibility to leakage and deformation. Moreover, using low grade energy such as waste heat from the PV panels to evaporate CO_2 in microchannel would be very effective. As such, in this present study, a microchannel evaporator configuration is modelled to ensure higher heat transfer.

2.4.2. Compressor

Compressor converts the low-pressure refrigerant to the required high-pressure condition. To attain the CO_2 supercritical pressure at the gas cooler, a CO_2 HP operates at a much higher compressor discharge pressure (CDP) (90-130 bar) compared to CFC/HFC HPs (10–40 bar). Such high CDP in a CO_2 HP can result in a significant mechanical loss as well as oil leakage. Different

compression mechanisms (e.g., reciprocating, rotary, and scroll) have been studied in terms of the compressor's performance and reliability.

Jiang et al. [63] studied a reciprocating compressor manufactured by the Dorin Company to analyze the impact of different compression cycles with and without internal heat exchanger (IHX). The results confirmed that the CDP, which was affected by the gas cooler outlet temperature, was always higher than the critical pressure of CO_2 (7.377 MPa), irrespective of the IHX use. Additionally, the Mitsubishi Company recently developed a commercial CO_2 compressor with a single rotary mechanism exclusively targeting residential HP applications [64]. In another study, Hiwata et al. [65] carried out a detailed study on a single-stage scroll compressor and compared its performance with their in-house built, two-stage rotary compressor. They reported that compression efficiency could be increased by adjusting the oil-injection rate in the compression chamber. Shimoji et al. [66] developed a prototype CO_2 scroll compressor for air conditioning based on R410A compressors and analyzed its basic quantitative losses through a simplified model. They found the volumetric and overall adiabatic efficiency reduced by 17% and 16%, respectively while dropping rotational speed from 3600 to 1800 RPM.

In terms of system configuration, the hermetic and semi-hermetic types are the recent research focus. In a study of a semi-hermetic compressor, Rozhentsev and Wang [67] reported that the HP performance was sensitive to even a marginal change in compressor efficiency and CDP. For example, at an optimum discharge pressure (85 bar), when the compressor efficiency decreased from 1 to 0.75, the overall HP performance reduced by 30% from the maximum COP of 4.5. However, they found the internal superheating had a minimal impact on the HP COP. Cavallini et al. [68] optimized a two-stage transcritical cycle using a semi-hermetic reciprocating compressor coupled with an intercooler. They reported the split-cycle with an integrated suction

line HX could increase the COP up to 25% compared to a baseline two-stage cycle. Zhang et al. [69] experimentally found that the volumetric efficiency of the single-stage compressor was higher than that of two-stage at compression ratios below 2.8, but the two-stage showed a higher volumetric efficiency at a compression ratio of 2.8 or higher. The isentropic efficiency had the same trend as volumetric efficiency. However, the DSH had a minimal effect on both volumetric and isentropic efficiencies for both configurations.

Recent studies have shown that, from a thermodynamics point of view, it is favorable to use a two-stage compressor in a transcritical CO_2 HP due to high working pressure. For water heating applications, Pitarch et al. [70] reported that the COP of the two-stage system was 11% higher than the single stage system. A commercially developed two-stage compressor for residential CO_2 HP water heaters equipped with an intermediate gas-injection mechanism between the first and second stages helped to reduce the vapor mixture losses [64]. It was found that such a two-stage configuration improved the compressor performance by 15% and 30% for compression ratios of 3 and 4, respectively. Similar to the two-stage design, Xing et al. [71] combined a high-pressure compressor and a low-pressure compressor using an IHX, and the simulation showed that the new design could attain 10 - 30% higher COP compared to a baseline system at a given evaporating temperature of -15 °C. Based on six different configurations of two-stage CO_2 refrigeration systems, Liu et al. [72] found that the gas cooler outlet temperature and the low-stage compressor significantly affect the system performance.

In the present study, a numerical model of a single-stage semi-hermetic compressor is used for simplicity. Since the compressor discharge pressure plays a pivotal role in the cycle efficiency, the compressor isentropic efficiency as a function of the compressor ratio is used to evaluate the compressor actual power consumption.

2.4.3. Gas Cooler

In a transcritical CO_2 heat pump, the heat rejection takes place at the supercritical temperature and pressure, and the optimum COP of the system is contingent upon the supercritical properties of CO_2 at the gas cooler [73]. A significant number of experimental and numerical studies can be found in the literature that has analyzed the supercritical CO_2 heat transfer characteristics in different types of channel geometries and arrangements. In this section, recent studies on the $scCO_2$ heat transfer mechanism in different HX configurations specifically for HP applications are presented. Additionally, different types of HX as a gas cooler and their effect on HP performance are analyzed.

Liao et al. [74] experimentally analyzed the heat transfer performance of supercritical CO_2 in a horizontal and inclined straight tube. The results showed that the heat transfer coefficient (HTC) was at the peak near the pseudo-critical region due to the enhanced specific heat capacity of CO_2. Moreover, the HTC increased when the bulk temperature was higher than the critical temperature for horizontal and vertical flow. They found the effect of buoyancy is more prominent in large diameter tubes than in mini-tubes, which causes a reduction in the supercritical CO_2 Nusselt number in a mini-channel. To account for the reduction in the Nusselt number, a new was proposed based on the experimental results. In a similar study, Dang et al. [75] suggested a modification of the Gnielinski correlation to predict the HTC of supercritical CO_2 in a circular, straight tube considering the effects of mass flux, heat flux, and tube diameter on HTC. Studies on horizontal circular tube-in-tube HXs showed that the HTC of supercritical CO_2 is a combination of free and forced convection because of the buoyancy effect close to the pseudo-critical vicinity [76, 77].

Helically coiled tubes HX were found to enhance supercritical CO_2 HTC compared to straight tubes HX [78, 79]. In helical structures, the centrifugal and buoyancy forces affect the flow field and heat transfer. The effect of buoyancy force can be ignored if the buoyancy number (Bo) is below 5.6×10^{-7} [80]. Forooghi et al. [81] further explained the buoyancy induced supercritical heat transfer in vertical and inclined tubes. At a significantly low buoyancy number (Bo $< 2.26 \times 10^{-6}$), the heat transfer deteriorates due to low near-wall turbulence, and the heat transfer starts to increase with the increase of the buoyancy effect due to a velocity gradient rise between the outer tube wall and the centerline.

A simulation of a finned tube gas cooler indicated that the flow field characteristics and heat transfer depend on the fin configuration, and a slit fin has higher HTC than a continuous fin for both the air-side and refrigerant-side, which improves heat rejection [82]. Li et al. [83] developed a low-cost fin and micro-channel integrated gas cooler and reported that the fin and micro-channel configuration could avoid air-side mal-distribution and had better performance at higher air velocities. Additionally, Garimella [84] and Chang et al. [85] proposed the use of near-counter-flow fin and tube type gas cooler.

Yang et al. [86] analyzed a multi-twisted-tube gas cooler where a counter-current double pipe copper HX was used as the gas cooler. In their HX configuration, the inner tubes were twisted together and fitted inside a larger tube. The theoretical and experimental results showed that a greater number of inner tubes increases the outlet water temperature, but, at the same time, the pressure drop increases sharply. Kim et al. [87] developed a multi-tube counter-flow gas cooler consisting of parallel smaller tubes bundled together inside a larger tube for a geothermal HP. In this configuration, the CO_2 and water flow in the opposite direction to ensure maximum heat transfer.

Compactness of the gas cooler is another key focus of recent research, which can be achieved by reducing refrigerant charge and tube size and varying the air volume flow rate. Marcinichen et al. [88] numerically studied these factors to reduce the size of an existing gas cooler used in a beverage vending machine. Chen et al. [89] analyzed the pinch point occurrence in a water-cooled CO_2 HP using the log mean temperature difference (LMTD) method and found that the gas cooler was undersized by 30% to 40%. Likewise, Sánchez et al. [90] developed a finite element model for properly sizing a CO_2 gas cooler. Yin et al. [91] developed and studied a compact gas cooler model using a finite element approach where the micro-channel gas cooler consisted of three passes of 13, 11, and 10 tubes. They found an increasing number of passes in the gas cooler might improve the performance, but the three-pass design is the best since there is not much difference between a five-pass and a three-pass gas cooler concerning the exit CO_2 enthalpy.

If the refrigerant mass flow rate is excessive, the specific volume of the refrigerant at the compressor inlet increases, which causes a high pressure-drop at the evaporator and a low specific enthalpy change at the gas cooler. Therefore, for the same compressor power consumption, the specific enthalpy exchange becomes less, and the system COP decreases. As such, Liu et al. [92] developed a genetic algorithm for maximizing CO_2 HP COP based on gas cooler pressure and the water flow rate. Similarly, to reduce the power consumption in real-time, Hu et al. [93] adopted an extremum seeking control (ESC) strategy considering the gas cooler pressure and outlet water temperature. A similar control strategy was developed by Peñarrocha et al. [94] to reduce the consumption by regulating the high-side pressure. by To optimize the performance of a CO_2 refrigeration system, Kim et al. [95] suggested a new control strategy. They utilized the difference between the required total HTC in the gas cooler for optimum COP and total HTC at any

concurrent gas cooler pressure. When the difference between the total HTCs is zero, the maximum COP is realized.

In the present study, a tube-in-tube type counter-flow gas cooler is modeled in which the CO_2 flows in the inner tube and water flows in the annulus of the tubes in the opposite direction of the CO_2 flow. In this configuration, the CO_2 and water flow in the opposite direction to ensure maximum heat transfer. While modeling the gas cooler the supercritical properties of CO_2 and the effect of pressure are taken into consideration.

2.4.4. Expansion Device

The prime functions of the expansion device in a CO_2 HP are to distribute CO_2 to the evaporator as well as to maintain a pressure difference between the evaporator and the gas cooler. Most of the recent investigations focused on different kinds of expansion device designs (e.g., ejectors, expansion valves) and their configurations in terms of the numerical modeling, geometrical structure, and system performance enhancement.

Theoretical and experimental investigations suggest that an ejector in place of an expansion valve can improve transcritical cycle performance [96, 97]. Zheng et al. [98] and He et al. [99] proposed dynamic numerical models, which are useful in predicting the dynamic system response in different operating conditions to optimize the ejector expansion performance. In a CO_2 transcritical cycle, expansion or throttling losses result in a low system performance. Such throttling losses can be overcome by adopting multi-ejector systems [71]. Furthermore, Boccardi et al. [100] experimentally studied the benefit of integrating a multi-ejector in a transcritical CO_2 cycle for heating applications. They found that the optimal multi-ejector configuration could reduce the throttling losses by 46%, and, thereby, improve the system performance by up to 30%.

In addition, the adjustable ejector configuration was found to enhance the system COP up to 30% compared to the fix-geometry ejector [101]. This was attributed to the fact that the adjustable ejector can provide a flexible control over the mass flow rate, which is the key to performance improvement. Lie et al. [102] performed a study to analyze the performance of an adjustable ejector for a simultaneous heating and cooling application. They found that an optimum heating and cooling performance can be achieved by regulating the ejectors' internal geometries. Xu et al. [103] made an effort to optimize the high-side pressure through an adjustable ejector, which uses a stepper motor moving a needle forward and backward to adjust the nozzle throat area. The study showed that such an ejector could regulate the throttling area for an optimal high-side pressure. The optimized pressure has a positive effect on the system performance and outweighs the low ejector efficiency.

Among many types of expansion devices, the electronic expansion valve (EEV) and capillary tubes have been studied for CO_2 HPs. Zhang et al. [104] experimentally studied the effect of the refrigerant charge amount and EEV opening on the performance of a CO_2 HP water heater. The EEV opening of 40% was found to be optimal for their system. Increasing the EEV opening from its optimal value to 60% decreased the heating capacity up to 30% due to an increase in the refrigerant charge and supercritical pressure, but the undercharged condition had a more severe consequence on the performance than an overcharged condition. Baek et al. [105] investigated the control methods of the gas cooler pressure in a CO_2 HP using an EEV. The EEV integrated CO_2 HP showed enhanced COP due to optimized pressure in the gas cooler. Besides EEV, capillary tubes are preferred as an expansion device particularly in small vapor compression refrigeration and air conditioning systems due to their simplicity, low initial cost, and low starting torque of compressor. Song et al. [106] found that the CO_2 HP using a capillary tube is promising with its

COP close to (above 80% of) that of a system using an EEV. In addition, in another study of CO_2 HP, Madsen et al. [107] found that the use of an adiabatic capillary tube was better than a fixed high-pressure expansion valve but inferior to an adjustable expansion valve. The study recommended the use of a capillary tube in transcritical CO_2 HP when the system is relatively small.

Based on the above discussion, there is room for improving the COP of the proposed system by using an expansion device instead of an expansion valve. As such, in the present study, the expansion device is modeled. In the expansion device the CO_2 pressure drops from the supercritical pressure to evaporator pressure without any work done on the refrigerant. As such, the enthalpy at the evaporator inlet remains same as the gas cooler outlet enthalpy.

2.5. Summary of Literature Review

A comprehensive review of the advances in CO_2 HP systems is presented in this section. Unlike CFCs/HFCs, CO_2 has no regulation liability because of its low GWP. Thermodynamically, the use of CO_2 as a working fluid is a feasible option in a transcritical cycle, as shown in the comparison between the subcritical and transcritical cycles.

In order to further improve the performance of the CO_2 HP system, research integrated renewable energy sources, other working fluids, and advanced control with a CO_2 system. The CO_2 GSHP cycle showed an equivalent performance as that of the conventional R134a and R22 HP cycles. Solar assisted CO_2 HP could attain a higher COP and reduce the electricity consumption compared to a baseline CO2 HP.

In terms of application, CO_2 HPs' applicability in a cold climate, despite a comparatively low COP, and their ability to provide the high-temperature hot water has made them one of the most promising technologies for the residential as well as industrial sectors.

Research has been playing a pivotal role in developing functional designs for HXs, expansion devices, and compressors to suit the CO_2 transcritical process. Most of the recent studies focus on the lightweight and compact microchannel HX designs since the two-phase and supercritical heat transfer of CO_2 is found to be enhanced in compact HXs. Additionally, microchannel HXs can sustain high working of CO2 and less vulnerable to leakage. In addition, the adjustable ejector and EEV as an expansion device was found to enhance the system COP compared to the fix-geometry expansion devices. To reduce the vapor mixture losses, studies have been carried out using multi-stage compressor equipped with an intermediate gas-injection mechanism. The two-stage transcritical cycle using a semi-hermetic reciprocating compressor is a very promising technology.

Drawing together the prior work on hybrid HPs and the benefits of using microchannels with CO_2, there is a promising option to develop a solar-assisted, CO_2 HP that utilized a microchannel HX attached to a PV array to evaporate the refrigerant. However, there exist no numerical studies on PV/microchannel evaporator integrated DXHP system using CO_2 as the working fluid.

3. OBJECTIVES OF THE THESIS

This study intends to accomplish the following objectives: (i) to develop a steady-state mathematical model of a new PV/microchannel evaporator integrated DXHP system using CO2 in a transcritical cycle, (ii) to use the model for a parametric study to analyze the effect of those parameters have on the system performance, (iii) to perform a sensitivity analysis to understand the relative significance of the operating parameters on the system performance parameters and to identify the dominant operating parameters of the system and, (iv) to use the model to investigate the seasonal performance of the system in Fargo, North Dakota weather conditions.

4. EVAPORATOR MODEL AND ANALYSIS

The following chapter has been submitted to the Journal of Applied Thermal Engineering for publication.

4.1. Evaporator Description

The PV/microchannel evaporator is sized to supply domestic hot water (>55 °C) for a four-membered single-family house in Fargo, North Dakota at a rate of 40 liters/person/day [108] and the construction is modeled to be represented of commercially available products and consistent with prior work. As shown by the cross-sectional view in Figure 4.1, the PV/microchannel evaporator has four main components: the PV panel, copper plate, microchannel copper tubes, and thermal insulation. Subsequently, 'evaporator' refers to the plate, tubes, and insulation collectively. The PV/microchannel evaporator geometric parameters are listed in Table 4.1. The PV panels are arranged in an array of 3×2 with 2 panels along the length of the microchannels as presented in Figure 4.2. The PV panel rests on the copper plate while the microchannel copper tubes are welded to the bottom of the copper plate. The PV panel length and width are chosen to be same as commercially available single-crystalline silicon cell PV panel having a reference efficiency of 15.4% and temperature coefficient of 0.0045 K^{-1} [109]. The microchannel tube diameter of 0.79 mm is selected to be consisted with previous studies [13, 110]. The spacing between two adjacent microchannel tubes is 30 mm. To minimize the heat losses from the evaporator, a phenolic foam insulation layer having a thickness of 62 mm and conductance of 0.02 $W \cdot m^{-1} \cdot K^{-1}$ [14] is provided beneath the microchannel tubes.
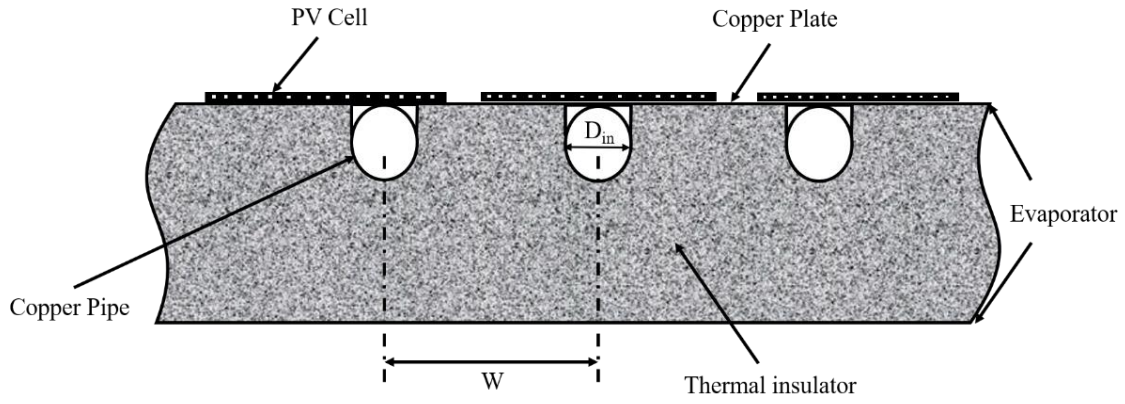
Figure 4.1: Cross-sectional view of PV/microchannel evaporator.
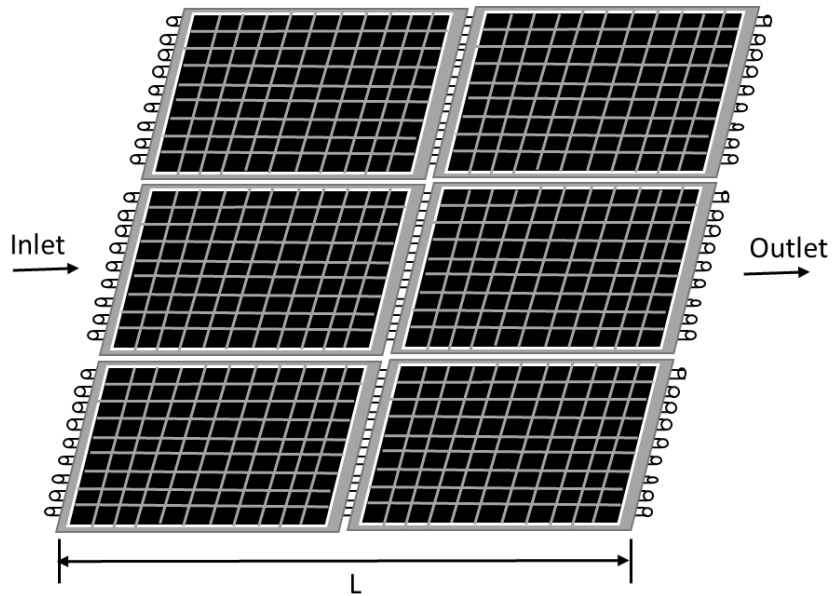
Figure 4.2: PV panel and microchannel evaporator arrangement.

Table 4.1: Parameters of the PV/microchannel evaporator.

Parameters	Value
PV Dimension	1.65 m×1 m
No. of PV panels	6 (2×3)
Diameter	0.79 mm
Number of Tubes	100
Tube Spacing	30 mm
Insulation thickness	62 mm
PV reference efficiency	15.4%
Temperature coefficient	0.0045
Absorptivity	0.90
Emissivity	0.96
Reflectivity	0.10
EVA transmittance	0.91
Bond conductance	30 $W \cdot m^{-1} \cdot K^{-1}$
Phenolic foam conductivity	0.02 $W \cdot m^{-1} \cdot K^{-1}$

4.2. Evaporator Mathematical Model

A steady state numerical model of the PV/microchannel evaporator is developed in this study. The mathematical model has two major sets of equations: energy balance equations of the PV panels and the evaporator, and conservation equations of the refrigerant.

4.2.1. Energy Balance Equations

The thermal resistance network of the PV/microchannel evaporator is shown in Figure 4.3. The excess heat from the PV panels is transmitted to the evaporator and passed to the refrigerant

flowing inside the microchannel evaporator. The contact resistance between the copper plates and copper pipes of the evaporator is neglected. The thermal contact resistance between the PV panels and the evaporator leads to a temperature differential between the PV panels (T_{pv}) and the evaporator (T_e). Since in a practical system the temperature of the PV panels, evaporator, and refrigerant vary along the flow direction due to pressure drop throughout the evaporator and refrigerant superheating at the evaporator outlet, in the present study, these equations are solved along the flow direction. Thus, the model's predicted temperatures are non-uniform in the flow direction while the temperatures are uniform at each cross-section, as would be expected for a uniform single pass evaporator.
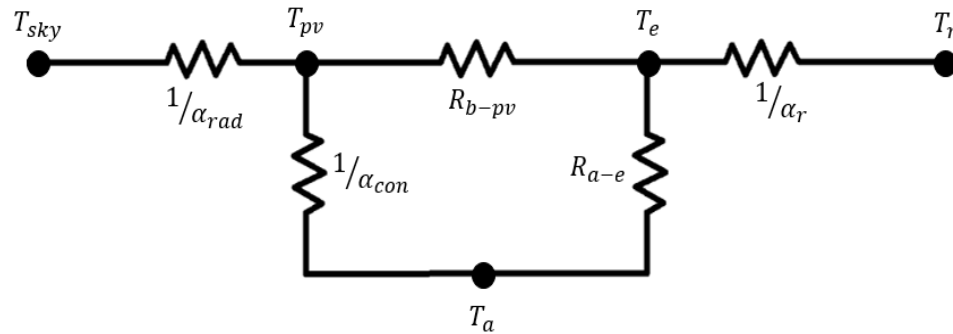
Figure 4.3: Thermal resistance network in the PV/evaporator.

The energy balance equation in the PV panels is as follows:

$$I_T(\tau\beta)_{PV} = E + \frac{T_{pv} - T_e}{R_{b-pv}} + \alpha_{rad}(T_{pv} - T_{sky}) + \alpha_{conv}(T_{pv} - T_a) \tag{1}$$

Part of the solar energy absorbed by the PV panels converts into electricity (E in Eq. 1) and the rest converts into heat energy. The electrical output (E) of the PV panels is calculated using Eq. 2, depends on the available solar insolation I_T and PV cell efficiency (η_{pv}).

$$E = I_T \tau_{eva} \eta_{pv} \tag{2}$$

The PV panel efficiency (η_{pv}) is dependent on the PV panel temperature (T_{PV}) and is given by Eq. 3, where, η_{ref} and κ are electrical efficiency and temperature coefficient, respectively, at solar insolation of 1000 W·m^{-2} and ambient temperature of 25 °C.

$$\eta_{PV} = \eta_{ref}\left[1 - \kappa\left(T_{PV} - T_{ref}\right)\right] \tag{3}$$

Part of the waste heat from the PV panels is transmitted to the evaporator (2nd term on the RHS of Eq. 1) and the remaining energy is lost to the ambient through radiation (3rd term on the RHS of Eq. 1) and convection (4th term on the RHS of Eq. 1).

For Eq. 1, the effective absorptivity ($\tau\beta$) of the PV panel, the radiation HTC (α_{rad}), the convective HTC (α_{conv}) to the ambient due to wind, and the relation between sky temperature (T_{sky}) and ambient temperature (T_a) are calculated according to the relationships from Duffie and Beckman, presented in Eq. 4 – Eq. 7.

$$(\tau\beta)_{PV} = \frac{\tau_{eva}\beta_{PV}}{1 - (1 - \beta_{PV}) \cdot r_{pv}} \tag{4}$$

$$\alpha_{rad} = \varepsilon_g \sigma\left(T_{PV}^2 + T_{sky}^2\right)\left(T_{PV} + T_{sky}\right) \tag{5}$$

$$\alpha_{conv} = 2.8 + 3.0 \cdot u_{wind} \tag{6}$$

$$T_{sky} = 0.0552 T_a^{1.5} \tag{7}$$

The energy balance equation of the evaporator is as follows:

$$A_{s,pv}\frac{\left(T_{pv} - T_e\right)}{R_{b-pv}} = A_r\alpha_r(T_e - T_r) + A_{s,e}\frac{(T_e - T_a)}{R_{a-e}} \tag{8}$$

Part of the waste energy absorbed by the evaporator is transmitted to the refrigerant (1st term on the RHS of Eq. 8) and the rest of the energy is lost to the ambient through the insulation layer (2nd term on the RHS of Eq. 8). The energy balance of the PV and evaporator are coupled to the conservation equations of the refrigerant through the refrigerant temperature (T_r) in Eq. 8.

33

4.2.2. Conservation Equations

The conservation equations of the refrigerant in the microchannel evaporator is expressed by nonlinear partial differential equations. The following assumptions are made while developing the conservation equations:

      I.   The flow in the evaporator is considered one-dimensional.

      II.   The changes in kinetic energy and potential energy are neglected.

      III.   No body force is acting on the refrigerant.

      IV.   Momentum does not change due to gravity.

To capture the change in refrigerant HTC and pressure drop due to refrigerant dry-out at higher vapor quality and superheated refrigerant flow, the refrigerant flow in the evaporator is divided into two-phase, dry-out, and superheated regions. In the two-phase region, a separated flow model is adopted to calculate the heat transfer and pressure drop. In the dry-out and superheated regions, the HTC and pressure drop are approximated using the vapor-only phase correlations, because by definition at the dry-out quality the cross-sectional area of the evaporator is occupied entirely by the vapor. The transition between the two-phase and dry-out regions is determined when the refrigerant quality exceeds the dry-out quality. The dry-out quality is calculated using a correlation developed by Maxime et al. [111] for CO_2 flow in microchannel shown in Eq. 9.

$$x_d = 1 - 338 Bo^{0.703} R_p^{1.43} \qquad (9)$$

In Eq. 9, R_p is the reduced pressure defined as a ratio of saturation pressure to the critical pressure, and Bo is the non-dimensional boiling number which represents a relation among the heat flux (q), refrigerant mass flux (G), and latent heat of vaporization (h_{fg}). The reduced pressure (R_p) and boiling number (Bo) are calculated from Eq. 10 and Eq. 11, respectively.

$$R_p = \frac{P_{sat}}{P_{crit}} \tag{10}$$

$$Bo = \frac{q}{Gh_{fg}} \tag{11}$$

4.2.2.1. *Two-phase flow*

To capture the realistic flow characteristics of the refrigerant in the two-phase region, a separated flow model is adopted. In the separated flow model, the relative velocity between the liquid and vapor is taken into account since vapor travels at a higher velocity than the liquid due to density difference.

The continuity equation of the refrigerant in the two-phase flow is shown in Eq. 12.

$$\frac{\partial}{\partial z}\left[(1 - \omega)\rho_f v_f + \omega \rho_g v_g\right] = 0 \tag{12}$$

In the continuity equation, v_g and v_f are the vapor and liquid velocity, respectively, given by:

$$v_f = \frac{xG}{\omega \rho_f} , \tag{13}$$

$$v_g = \frac{xG}{\omega \rho_g} , \tag{14}$$

where ω is the void fraction defined as the cross-sectional area of the microchannel occupied by the vapor in the two-phase region. The void fraction (ω) is calculated using an empirical correlation (Eq. 15) developed by Permoli et al. [112] utilizing the slip ratio (s).

$$\omega = \frac{1}{1 + s\left(\frac{1 - x}{x}\right)\left(\frac{\rho_g}{\rho_f}\right)} \tag{15}$$

35

The slip ratio (s) is defined as the ratio of the velocity of vapor to liquid in the two-phase region. For a homogeneous flow model, slip ratio is 1 meaning there is no relative velocity between liquid and vapor. The slip ratio (s) is calculated using a correlation (Eq. 16) developed by Chisholm [113].

$$s = \left[1 - x \left(1 - \frac{\rho_f}{\rho_g} \right) \right]^{1/2} \tag{16}$$

The momentum equation of the refrigerant in the two-phase flow is shown in Eq. 17.

$$\frac{\partial P}{\partial z} = \left(\frac{dp}{dz} \right)_m + \left(\frac{dp}{dz} \right)_{tp} \tag{17}$$

In the momentum equation, the two-phase momentum pressure drop, $\left(\frac{dp}{dz} \right)_m$, is calculated using Eq. 18, and the two-phase frictional pressure drop, $\left(\frac{dp}{dz} \right)_{tp}$, is calculated utilizing Eq. 19.

$$\left(\frac{dp}{dz} \right)_m = -G^2 \frac{d}{dz} \left[\frac{(1-x)^2}{\rho_f (1-\omega)} + \frac{x^2}{\rho_g \omega} \right] \tag{18}$$

$$\left(\frac{dp}{dz} \right)_{tp} = \varphi_f^2 \left(\frac{dp}{dz} \right)_f \tag{19}$$

In Eq. 19, φ_l^2 is the two-phase frictional multiplier given by Chisholm [114].

$$\varphi_f^2 = 1 + \frac{C}{X} + \frac{1}{X^2} \tag{20}$$

In Eq. 20, the Chisholm parameter, C is calculated using the correlation developed by Yun et al. [115] for two-phase CO_2 flow in a microchannel.

$$C = 21 \times (1 - e^{-1.95 D_{in}}) \tag{21}$$

In Eq. 20, X is the Lockhart–Martinelli parameter (L-M) [116], which encompasses the effect of quality, density, and viscosity on the heat transfer characteristics, calculated using Eq. 22.

$$X = \left(\frac{\mu_f}{\mu_g}\right)^{1/8} \cdot \left(\frac{1-x}{x}\right)^{7/8} \cdot \left(\frac{\rho_g}{\rho_f}\right)^{1/2} , \tag{22}$$

In Eq. 19, $\left(\frac{dp}{dz}\right)_f$ is the frictional pressure drop for liquid-only phase which is dictated by the frictional coefficient (f_f).

$$\left(\frac{dp}{dz}\right)_f = -f_f \left(\frac{4}{D_{in}}\right)\left(\frac{1}{2}\frac{G^2(1-x)^2}{\rho_f}\right) \tag{23}$$

The frictional coefficient (f_f) is evaluated using Eq. 24 for laminar flow and Eq. 25 for turbulent flow for flow inside the microchannel.

$$f_f = \frac{16}{Re_f}, \quad Re < 2300 \tag{24}$$

$$f_f = \frac{0.079}{Re_f^{0.25}}, \quad Re \geq 2300 \tag{25}$$

In the two-phase region, the Reynolds number (Re) is calculated using vapor quality (x) as shown in Eq. 26.

$$Re_f = \frac{G(1-x)D_{in}}{\mu_f} \tag{26}$$

The energy equation of the refrigerant in the two-phase flow is given in Eq. 27

$$A_{s,e}G\frac{\partial h}{\partial z} = \pi D_{in}\alpha_r(T_e - T_r) \tag{27}$$

In the energy equation, α_r is the refrigerant HTC in the two-phase region. Heat transfer in microchannel with two-phase flow is governed by two mechanisms: nucleate boiling and forced convection. The heat transfer correlation (Eq. 28) developed by Chen et al. [117] quantifies both the mechanisms.

$$\alpha_r = S \cdot \alpha_{nb} + F \cdot \alpha_f \tag{28}$$

In Eq. 28, S and F are two dimensionless factors termed the nucleate boiling suppression factor and Reynolds number factor (convective two-phase multiplier), respectively. To calculate

the nucleate boiling suppression factor (S), a modified correlation (Eq. 29) developed by Choi et al. [118] for CO_2 is used.

$$S = 7.2694\left(\varphi_f^2\right)^{0.0094} \cdot Bo^{0.2814} \tag{29}$$

For the nucleate boiling HTC, a correlation (Eq. 30) developed by Cooper [119] is used to be consistent with Choi et al. [118], where M is the molecular weight of the refrigerant and in the present model, M = 44.

$$\alpha_{nb} = 55R_p{}^{0.12}\left(-0.4343l\,n(R_p)\right)^{-0.55} \cdot M^{-0.5} \cdot q^{0.67} \tag{30}$$

The modified Reynolds number factor (F) developed by Choi et al. [118] from their experimental study of heat transfer in two-phase flow of CO_2 (Eq. 31) is used in this study, because this modification accounts for the convective heat transfer appearing later for CO_2 compared to conventional refrigerants due to nucleate boiling.

$$F = 0.05\varphi_f^2 + 0.95 \tag{31}$$

For the convective HTC of the liquid-only phase, the Dittus-Boelter correlation is used as presented in Eq. 32.

$$\alpha_f = 0.023\frac{k_f}{D_{in}}\left[\frac{G(1-x)D_{in}}{\mu_f}\right]^{0.8}\left(\frac{C_{pf}\mu_f}{k_f}\right)^{0.4} \tag{32}$$

In Eq. 32, k and μ are the thermal conductivity and dynamic viscosity of the refrigerant respectively.

4.2.2.2. Dry-out and Superheated Regions

In the dry-out and superheated regions, the conservation equations are developed based on single-phase vapor-only flow. The continuity equation of the refrigerant in the dry-out and superheated regions is shown is Eq. 33.

$$\frac{\partial \dot{m}_r}{\partial z} = 0 \tag{33}$$

The momentum equation of the refrigerant in the dry-out and superheated regions is shown in Eq. 34.

$$\frac{\partial P}{\partial z} = -\left(\frac{dp}{dz}\right)_g \tag{34}$$

In the dry-out and superheated region, the pressure drop is dominated by the frictional pressure drop, $\left(\frac{dp}{dz}\right)_g$, since there is no slip between the phases and calculated using Eq. 35.

$$\left(\frac{dp}{dz}\right)_g = f_g \frac{2G^2}{D_{in}\rho_g} \tag{35}$$

In Eq. 35, f_g is the vapor-only phase frictional coefficient calculated using Eq. 36.

$$f_g = [1.82 \, log(Re) - 1.64]^{-2} \tag{36}$$

The energy equation of the refrigerant in the dry-out and superheated regions is shown in Eq. 37.

$$A_{s,e} G \frac{\partial h}{\partial z} = \pi D_{in} \alpha_r (T_e - T_r) \tag{37}$$

In the energy equation, α_r is the local HTC calculated using Dittus-Boelter's correlation for single-phase flow.

$$\alpha_r = 0.023 Re_g{}^{0.8} Pr^{0.4} \frac{k_g}{D_{in}} \qquad (38)$$

Here, the local HTC (α_r) depends on the thermal conductivity of refrigerant (k), the inner diameter of the evaporator (D_{in}), and two dimensionless parameters: the Reynolds number (Re) and the Prandtl number(Pr).

4.3. Evaporator Numerical Simulation and Model Validation

4.3.1. Numerical Simulation

The finite difference method was utilized to discretize the nonlinear partial differential equations and an explicit scheme was used to solve the equations. The numerical code was developed in MATLAB. The thermophysical properties and transport properties of CO_2 were obtained from REFPROP 9.1. The model solves the governing equations at each discretized point in the evaporator until the PV panel temperature (T_{pv}) and the evaporator temperature (T_e) converge with a residual $< 10^{-3}$ °C. As illustrated by Figure 4.4, this small residual does not affect the model predictions as the temperatures are stable at residuals $< 10^{-3}$ °C.

(a)   (b)
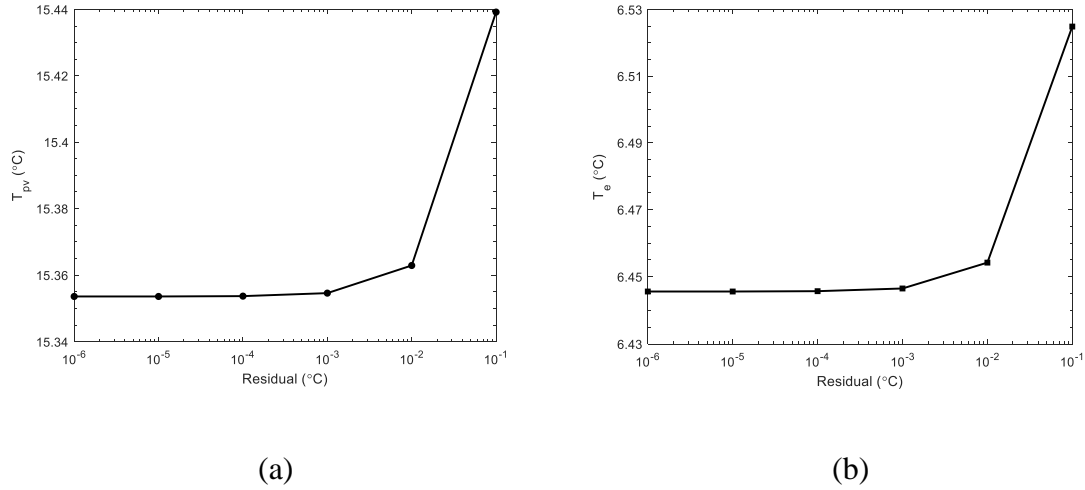
Figure 4.4: Model predicted PV panel temperature (T_{pv}) and evaporator temperature (T_e) as a function of residual size.

4.3.2. Model Validation

The developed numerical model is validated through internal and external checking. The internal checking is performed to make sure that the mass, momentum, and energy are conserved throughout the system. Additionally, a mesh refinement study as shown in Figure 4.5 is done to make sure that the mesh size is small enough so that there is no discontinuity in the refrigerant properties. As shown by Figure 4.5, the quality of the refrigerant is constant for mesh number over 200. This result for quality is consistent with other properties and outputs (e.g. pressure drop). Thus, a mesh number of 400 was used to ensure all the simulations are in the constant region.
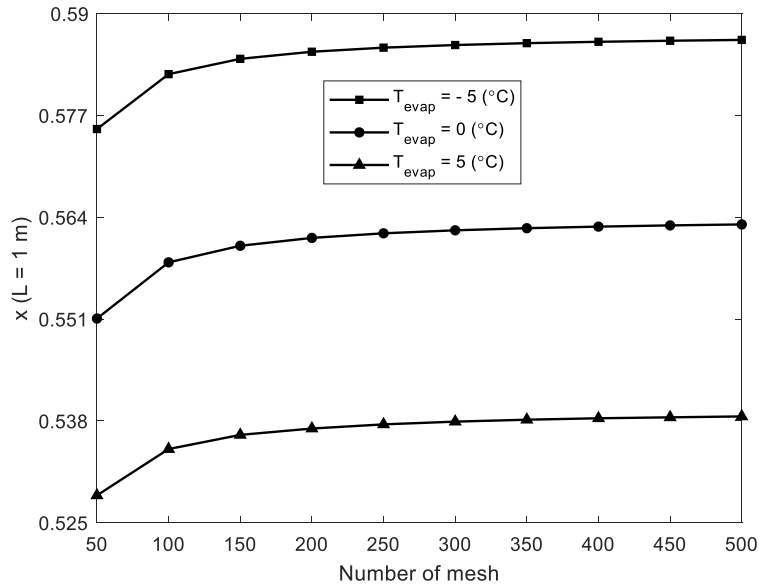
Figure 4.5: Evaporator mesh study.

The external checks are performed comparing the HTC and pressure drop predicted by the model with experimental results from available literatures. Figure 4.6a shows the calculated and experimental HTC [120] plotted against vapor quality. The model predicts the HTC within root mean square deviation (RMSD) of 14.60% for a refrigerant mass flux of 300 $kg \cdot m^{-2} \cdot s^{-1}$ and 7.80% for a mass flux of 600 $kg \cdot m^{-2} \cdot s^{-1}$ compared to the experimental work of Linlin et al. [120]. Figure 4.6b shows the calculated and experimental pressure drop [121] plotted against vapor quality. The model predicts the pressure drop within RMSD of 21.40% for a refrigerant mass flux of 190 $kg \cdot m^{-2} \cdot s^{-1}$ and 18.70% for a mass flux of 280 $kg \cdot m^{-2} \cdot s^{-1}$ compared to the experimental work of Pettersen et al. [121]. Based on the internal and external checks, it was determined that the model accuracy is enough to investigate the model.

(a)
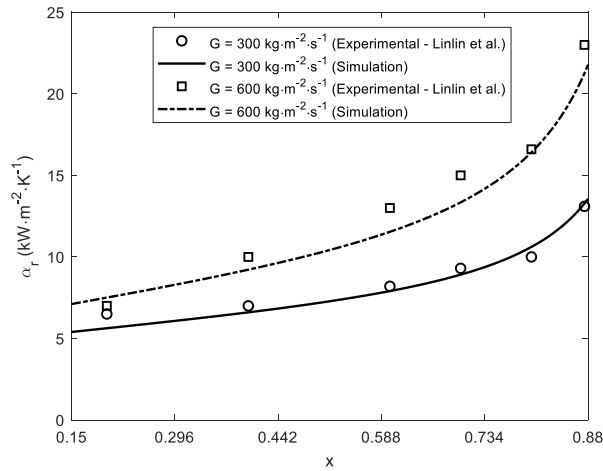
(b)
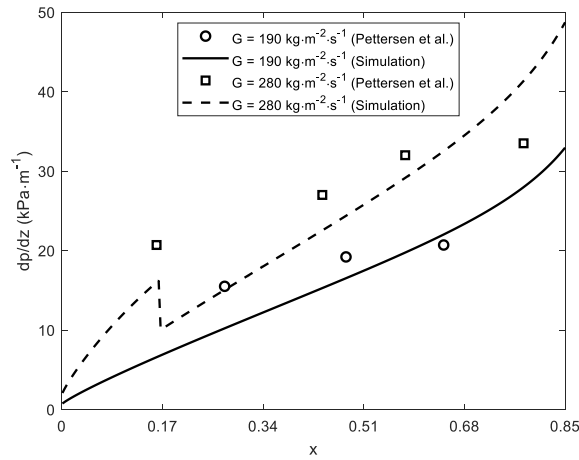
Figure 4.6: Comparison of simulation results with reference studies: CO_2 pre-dryout two-phase (a) HTC at $q = 7.5$ kW·m^{-2} and $T_{evap} = -10$ °C [120], (b) pressure drop at $q = 10$ kW·m^{-2} and $T_{evap} = 0$ °C [121].

4.4. Scope of the Evaporator Study

In this study, the variables considered are solar insolation, degree of superheating, refrigerant mass flux, and evaporation temperature. Each variable has a baseline value and a range. The simulations run through the range of a variable while holding all the other variables at the baseline values. The baseline solar insolation (500 W·m^{-2}) was determined by averaging weather data from NREL typical metrological year 3 (TMY3) [122] between 9 AM to 3 PM from March to October for Fargo, North Dakota. The ambient temperature (16 °C) and the wind speed (4.84

m·s^{-1}) were determined in the same manner but are held constant for all simulations. A baseline superheating of 5 °C at the evaporator outlet is used to ensure no liquid refrigerant enters the compressor [123]. The baseline refrigerant mass flux was chosen so that the full heat pump system can heat the daily domestic supply water for a family of four to a temperature > 55 °C, which is in the range specified for domestic hot water (DHW) temperatures in US residential buildings [15]. The baseline evaporation temperature is 0 °C, which is consistent with the optimum temperature found by Sarkar et al. [124] for a CO_2 heat pump. The variable parameters range and baseline values are summarized in Table 4.2.

Table 4.2: Variable parameter ranges and baseline values.

Variables	Ranges	Base Values
Solar insolation	200 to 1000 W·m^{-2}	500 W·m^{-2}
Degree of superheating	0 to 25 °C	5 °C
Refrigerant mass flux	300 to 700 kg·m^{-2}·s^{-1}	430 kg·m^{-2}·s^{-1}
Evaporating temperature	-15 to +15 °C	0 °C

4.5. Evaporator Results and Discussion

The objective is to identify conditions that maximize CO_2 heat absorption and minimize pressure drop while preventing subcooling at the evaporator inlet and restricting the CO_2 temperature to be lower than the evaporator temperature. To help interpret the subsequent results, the HTC and pressure variation along the length of the evaporator is presented in Figure 4.7 and Figure 4.8.

Figure 4.7a shows the HTC variation in the microchannel evaporator at the baseline operating conditions. In the two-phase flow region ($x < x_d$), the HTC increases gradually due to an

increase in convective heat transfer at higher vapor quality. At the dry-out quality ($x = x_d$), the HTC has a sharp increase to its peak value due to an abrupt increase in the two-phase convective heat transfer multiplier (φ_f^2). At qualities higher than the dry-out quality ($x > x_d$), the HTC reduces to a vapor-only phase HTC, which is much lower compared to the two-phase HTC due to reduced CO_2 density and specific heat. Figure 4.7b shows the HTC variation in the microchannel evaporator at various degrees of superheating at the evaporator outlet. The degree of superheating has a very strong effect on the location of the dry-out occurrence and the dry-out HTC. The variation of HTC at the evaporator inlet ($L = 0$ m) is due to changes in the degree of superheating which causes the evaporator inlet vapor quality to change. At higher inlet qualities, the convection heat transfer contribution increases, and subsequently, the HTC is higher. Figure 4.7c shows the average HTC variation in the microchannel evaporator at various degrees of superheating at the evaporator outlet. The average HTC decreases with an increase in the degree of superheating at the evaporator outlet due to an early transition to vapor-only flow. At the baseline operating parameters of $G = 430$ kg·m^{-2}·s^{-1}, $T_{evap} = 0$ °C, and $I_T = 500$ W·m^{-2}, increasing the degree superheating from 0 to 25 °C changes the location of dry-out occurrence from 3.20 to 1.38 m from the evaporator inlet, and decreases the average HTC from 7.74 to 5.23 kW·m^{-2}·K^{-1}, respectively.
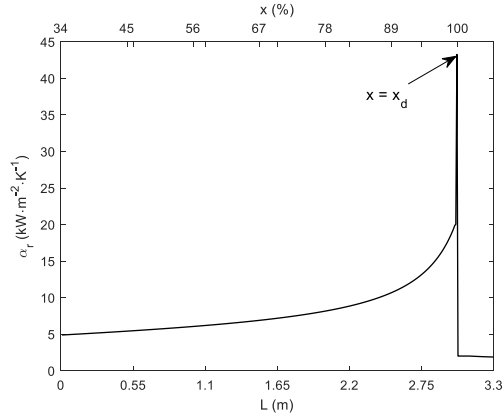
(a)
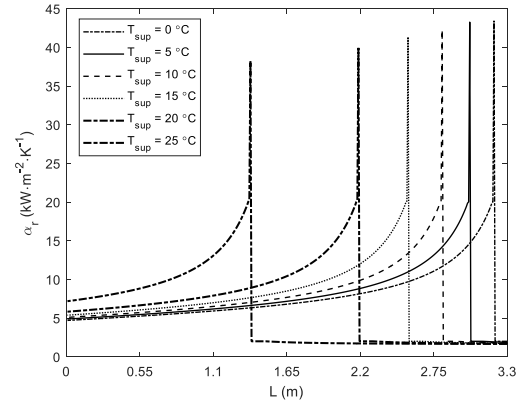
(b)
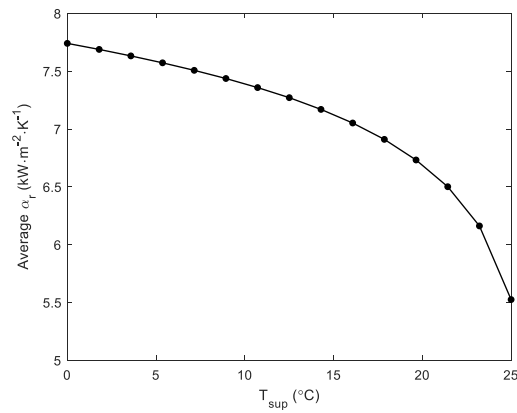
(c)

Figure 4.7: (a) The HTC along the length of the evaporator at the baseline operating conditions (b) the HTC along the length of the evaporator at a different degree of superheating at $G = 430 \text{ kg·m}^{-2}\text{·s}^{-1}$, $T_{evap} = 0$ °C, and $I_T = 500 \text{ W·m}^{-2}$, (c) the average HTC variation with changing the degree of superheating at the evaporator outlet at $G = 430 \text{ kg·m}^{-2}\text{·s}^{-1}$, $T_{evap} = 0$ °C, and $I_T = 500 \text{ W·m}^{-2}$.

Figure 4.8a shows the pressure distribution in the microchannel evaporator at the baseline operating conditions. In the two-phase region ($x < x_d$), the drop in pressure is due to frictional loss and change in momentum. In the two-phase region, the frictional pressure drop contribution to the total pressure drop compared to the pressure drop due to momentum change is higher. The frictional pressure drop is higher because at the baseline operating conditions the CO_2 flow is laminar in the two-phase region. In the dry-out ($x \geq x_d$) and superheated regions, there is little

46

change in pressure. The frictional pressure drop is lower compared to the two-phase frictional pressure drop due to turbulent flow as well as lower density and lower viscosity of the vapor. Figure 4.8b shows the pressure variation along the length of the evaporator at varying mass flux and at $T_{sup} = 5$ °C, $T_{evap} = 0$ °C, and $I_T = 500$ W·m^{-2}. The pressure drop increases with the increase in CO_2 mass flux due to a simultaneous increase in frictional loss and momentum pressure drop. At $T_{sup} = 5$ °C, $T_{evap} = 0$ °C, and $I_T = 500$ W.m^{-2}, changing the CO_2 mass flux from 300 to 700 kg·m^{-2}·s^{-1} increases the pressure drop from 124.83 to 458.78 kPa, respectively.

(a)   (b)
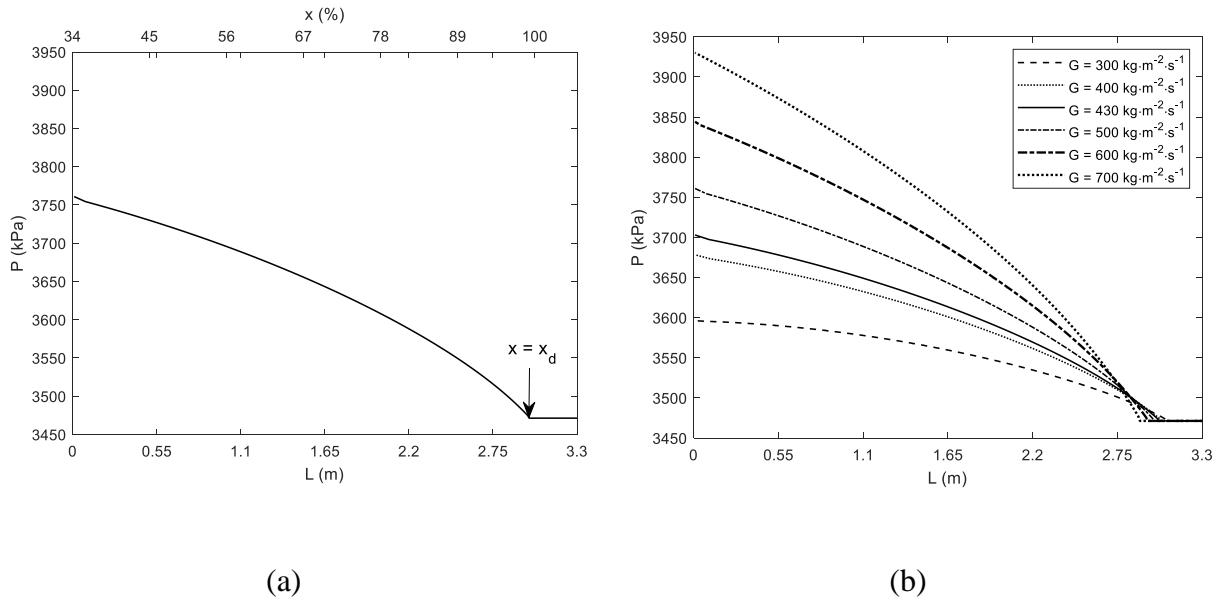
Figure 4.8: CO_2 pressure distribution along the length of the evaporator (a) at the baseline operating condition (b) at varying mass flux and at $T_{sup} = 5$ °C, $T_{evap} = 0$ °C, and $I_T = 500$ W·m^{-2}.

47

<p style="text-align:center">(a)   (b)</p>
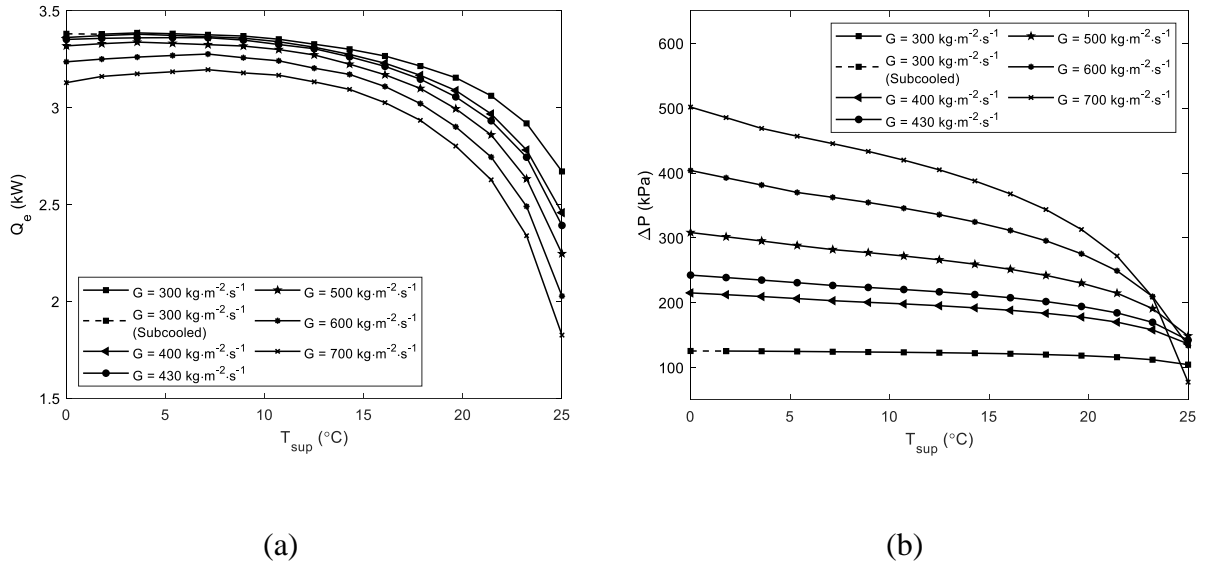
Figure 4.9: Effect of degree of superheating on the (a) heat absorption (b) pressure drop at $T_{evap} = 0$ °C and $I_T = 500$ W·m^{-2}.

The effects of degree of superheating, CO_2 mass flux, and evaporation temperature on the heat abortion and pressure drop is discussed below based on the HTC and pressure drop analysis made on Figure 4.7 and Figure 4.8. Figure 4.9 illustrates the effect of the degree of superheating on the heat absorption and pressure drop at different refrigerant mass flux. From Figure 4.9, the CO_2 heat absorption is relatively constant for superheating up to 10 °C for all the CO_2 mass flux. For example, increasing the degree of superheating from baseline to 10 °C while holding the other operating parameters at baseline, the heat absorption decrease is less than 1%. Further increasing the superheating over 10 °C results in the reduction of heat absorption for all the CO_2 mass flux due to reduced HTC (Figure 4.7). As shown in Figure 4.9a, increasing superheating from 10 to 25 °C at baseline operating conditions, the heat absorption decreases by 28%. Increasing the mass flux, decreases heat absorption because for a constant outlet condition (e.g. degree of superheating) the inlet quality increases. For example, increasing the CO_2 mass flux from 300 to 700 kg·m^{-2}·s^{-1} while holding the other parameters at the baseline conditions, the heat absorption decreases from

3.38 to 3.19 kW, respectively. From Figure 4.9b, the pressure drop decreases with the increase in superheating due to both an early transition to vapor-only flow (Figure 4.7) and the vapor region having a lower pressure drop (Figure 4.8). For example, at $G = 700\ \text{kg·m}^{-2}\text{·s}^{-1}$ increasing superheating from 0 to 25 °C, the pressure drop decreases from 501.66 kPa to 77.40 kPa, respectively. However, at low mass flux, this reduction in pressure drop is insignificant. For example, at $G = 300\ \text{kg·m}^{-2}\text{·s}^{-1}$, for the superheating of 0 °C and 25 °C, the difference between the pressure drops is only 21.04 kPa. By contrast, increasing the mass flux at all the superheating temperature increases pressure drop (Figure 4.8).

(a)   (b)
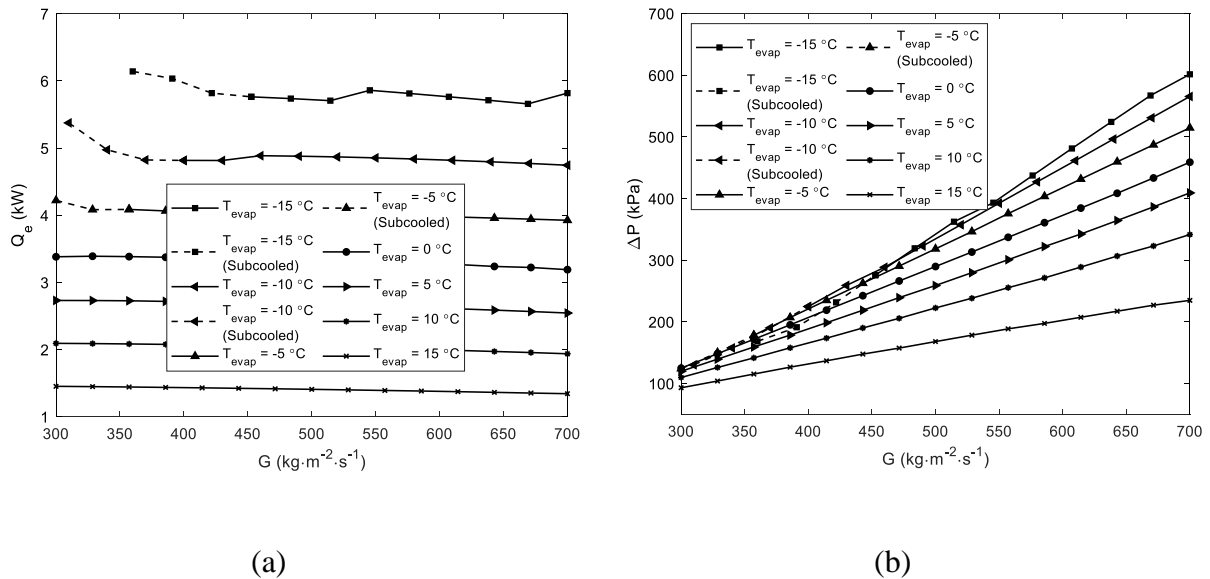
Figure 4.10: Effect of CO_2 mass flux on the (a) heat absorption (b) pressure drop at $T_{sup} = 5$ °C and $I_T = 500\ \text{W·m}^{-2}$.

Figure 4.10 shows the effect of CO_2 mass flux on the heat absorption and pressure drop at various evaporation temperatures. From Figure 4.10a, it can be seen that the variation of mass flux has a little effect on the heat absorption at each evaporation temperature. As the evaporation temperature decreases, the CO_2 heat absorption increases due to the higher temperature difference between the refrigerant and the evaporator. Decreasing the evaporation temperature from the

49

baseline to - 15 °C while holding the other operating parameters at baseline conditions, the heat absorption increases from 3.37 to 5.85 kW, respectively. Decreasing evaporation temperature also results in a reduction in the evaporator inlet quality, and at a low CO_2 mass flux, the evaporator inlet condition becomes a subcooled liquid. For example, at - 5 °C of evaporation temperature and a CO_2 mass flux of 350 $kg \cdot m^{-2} \cdot s^{-1}$, the evaporator inlet condition is saturated liquid (x = 0). Decreasing evaporation temperature below - 5 °C or mass flux below 350 $kg \cdot m^{-2} \cdot s^{-1}$ results in subcooling at the evaporator inlet, which is not suitable for a heat pump operation since subcooling at the evaporator inlet corresponds to a much higher gas cooler pressure [125]. These higher pressures are expected to reduce the COP of a heat pump system. With a low mass flux (e.g. 300 $kg \cdot m^{-2} \cdot s^{-1}$) and an evaporation temperature below - 10 °C, the evaporator inlet is too deep in the subcooled region, where CO_2 thermodynamic data is not available (CO_2 temperature < - 56.5 °C). From Figure 4.10b, increasing the CO_2 mass flux increases pressure drop (Figure 4.8). Decreasing evaporation temperature also increases the pressure drop and it is more prominent at higher CO_2 mass flux. For example, for G = 700 $kg \cdot m^{-2} \cdot s^{-1}$ decreasing the evaporation temperature from 0 to - 15 °C causes the pressure drop to increase by 142.58 kPa, whereas for G = 430 $kg \cdot m^{-2} \cdot s^{-1}$, the pressure drop increase is only 7.16 kPa.
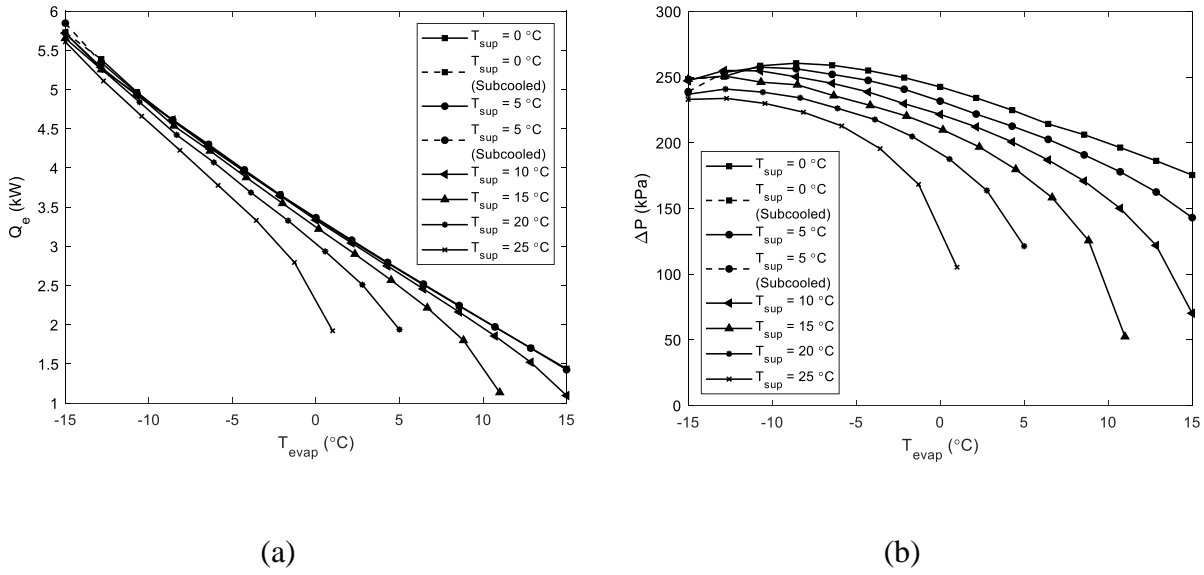
Figure 4.11: Effect of evaporation temperature on the (a) heat absorption (b) pressure drop $G =$ 430 kg·m^{-2}·s^{-1} and $I_T = 500$ W·m^{-2}.

Figure 4.11 illustrates the effect of CO_2 evaporation temperature on the heat absorption and pressure drop at various degrees of superheating. From Figure 4.11a, the heat absorption increases with a decrease in evaporation temperature due to the increased difference between evaporator temperature and refrigerant temperature. While holding the other operating parameters at the baseline, increasing evaporation temperature from 15 to -15 °C increases the heat absorption from 1.43 to 5.58 kW, respectively. At all the evaporation temperatures, the heat absorptions are comparable up to 10 °C of superheating. However, superheating over 10 °C reduces the heat absorption and this reduction is more prominent at higher evaporation temperature (e.g. 5 °C). For evaporation temperature > 5 °C and superheating > 15 °C, the evaporator temperature is lower than the refrigerant temperature and as a result, the CO_2 cannot absorb heat. From Figure 4.11b, increasing the evaporation temperature reduces the pressure drop and the reduction is more prominent at higher evaporation temperature (e.g. 5 °C). However, at 0 and 5 °C of superheating,

51

there is a slight increase in pressure drop as the evaporation temperature increases from -15 to -10 °C because of subcooled liquid CO_2 flow in part of the evaporator.

From the results of Figure 4.9 - Figure 4.11 and considering the practical limitations of using a PV/microchannel evaporator in a heat pump system, some broad observations can be drawn on the recommended degree of superheating, mass flux, and evaporation temperature. Superheating over 10 °C reduces the heat absorption (Figure 4.9a). Practically, the refrigerant should exit the evaporator as a superheated vapor, rather than as saturated vapor, to ensure no liquid refrigerant enters the compressor. As such, 5 - 10 °C of superheating is recommended to maximize the heat absorption while ensuring no liquid refrigerant is entering the compressor. The mass flux has a minimal impact on the heat absorption for superheating between 5 - 10 °C (Figure 4.9a and Figure 4.10a), but a lower mass flux is desired to minimize the pressure drop (Figure 4.10b). A lower evaporation temperature is also desired to maximize the heat absorption (Figure 4.11a). However, at the lowest flux rates and low evaporation temperatures, the CO_2 is a subcooled liquid at the evaporator inlet (Figure 4.10a). Such condition causes a heat pump discharge pressure to increase and, thus, is expected to reduce the overall system performance [125]. Additionally, the pressure drop increases with a lower evaporation temperature (Figure 4.11b) especially at a higher mass flux (Figure 4.10b). As a balance between these competing effects, it is recommended that CO_2 mass flux rates between $350 – 550$ $kg \cdot m^{-2} \cdot s^{-1}$ and evaporation temperatures between +5 to -5 °C be investigated at the system level analysis.
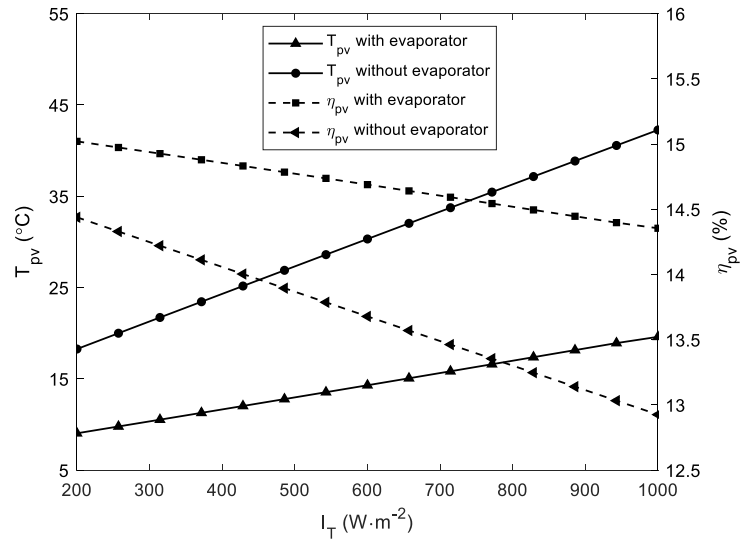
Figure 4.12: Comparison of PV temperature and electrical efficiency with and without microchannel evaporator.

The PV temperature, with and without the microchannel evaporator, versus solar insolation is shown in Figure 4.12. Due to the cooling effect of evaporating the CO_2, the PV temperature with the evaporator is always lower than the PV temperature without the microchannel evaporator. At an insolation of 200 W·m^2, the PV temperature with the evaporator is 10 °C cooler. At 1000 W·m^2, it is 23 °C cooler. The temperature difference between the PV with and without the evaporator is higher at higher solar isolation because the CO_2 absorbs more waste heat from the PV panel. For example, the heat absorbed is 2.23 kW at the solar insolation of 200 W·m^{-2}, whereas it is 5.35 kW at 1000 W·m^{-2}. This cooling effect and the resulting lower PV cell temperature results in higher PV efficiency. At an insolation of 200 W·m^2, the PV efficiency is 15.02% with the evaporator and 14.44% without the evaporator. This difference in efficiencies is accentuated at higher insolation levels because of the increased difference between the PV temperature with and without the evaporator. For example, at an insolation of 1000 W·m^2, the PV efficiency is 14.35% with the evaporator and 12.93% without the evaporator.

4.6. Evaporator Study Summary

Analysis of the PV/microchannel evaporator showed that for a baseline solar insolation of 500 W·m^{-2}, a 5 - 10 °C of superheating at the evaporator outlet, an evaporator temperature between - 5 to + 5 °C, and a CO_2 mass flux of 350 – 550 kg·m^{-2}·s^{-1} balances the heat absorption while minimizing the pressure drop. Increasing the degree of superheating reduces the pressure drop, and at low refrigerant mass flux this effect is minimized. If evaporation temperature is over 5 °C, a high degree of superheating can lead the CO_2 temperature to be higher than the evaporator temperature. If the evaporation temperature is lower than -5 °C, a low mass flow rate can result in CO_2 subcooling at the inlet. At each evaporation temperature, the variation of mass flux has a very minimal effect on the heat absorption due to change in inlet quality. However, the pressure drop increases with mass flux and is more prominent at low evaporation temperatures. Even though increasing the evaporation temperature has a positive effect on the pressure drop, it also decreases heat absorption.

For the PV, it is determined that the evaporation temperature has a significant effect on the PV temperature, and hence on the electrical efficiency. The cooling effect of the microchannel evaporator on the PV panels is prominent at higher insolation level. For example, at an insolation level of 1000 W·m^{-2}, a 23 °C reduction in PV cell temperature is possible, corresponding to a 1.42% absolute increase in PV efficiency. At the baseline operating conditions, the PV temperature reduced by 15 °C which resulted in an absolute PV efficiency increase of 0.90%.

5. HEAT PUMP WATER HEATER

A manuscript is being developed from chapter 5 to 9 to be submitted to a peer-reviewed journal for publication.

5.1. Heat Pump Description

A schematic diagram of the PV/microchannel integrated heat pump along with the PV/evaporator configuration is presented in Figure 5.1. The heat pump system consists of four major components: PV/microchannel evaporator module; a variable speed compressor; a gas cooler; and an expansion device. As detailed in section 4.1, the PV/microchannel evaporator has three main components: the PV panel, copper plate, and microchannel copper tubes. The evaporator is sized to supply domestic hot water (> 55 °C) for a four membered single-family house in Fargo, North Dakota at a rate of 40 liters/person/day [108]. The PV panels are arranged in an array of 3×2 with 2 panels along the length of the microchannels. The evaporator inlet and outlet are connected with headers. The inlet header splits the CO_2 flow from expansion device to the microchannel tubes. The outlet header accumulates the CO_2 from the microchannel tubes and passes the CO_2 to the compressor. The gas cooler is a single-pass, counter-flow, tube-in-tube-type heat exchanger, which transfers heat from the CO_2 to the water. The heat pump operation requires electrical energy to run the compressor, which can be supplied by the PV modules using an inverter. The heat pump operates only a few hours a day while the PV modules generate electricity all day long. The PV generated electricity can be stored in batteries or feed into the local grid during the time when the heat pump is not in operation.
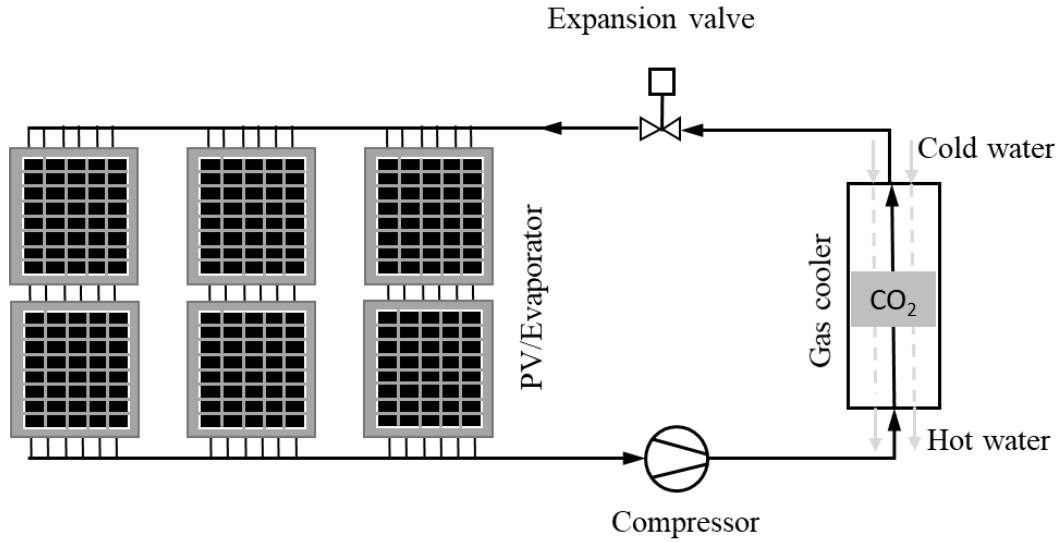
Figure 5.1: Schematic diagram of the heat pump with PV panel arrangement

5.2. Heat Pump Mathematical Model

The mathematical model of the PV/microchannel integrated DXHP is described in five different sections: evaporator, compressor, gas cooler, expansion valve, and system performance and sensitivity analysis.

5.2.1. Evaporator

Chapter 4.1 details the structure and geometry of an individual evaporator panel. Chapter 4.2 describes the evaporator mathematical model in detail. The full system model uses the same evaporator model. The heat pump uses the same evaporator described in chapter 4.1.

5.2.2. Compressor

The model assumes that the compressor is semi-hematic and adiabatic. Equation 39 shows the power consumption of the adiabatic compressor.

$$W_c = \frac{W_{isen}}{\eta_{isen}} \tag{39}$$

The ideal isentropic power consumption (W_{isen}) by the compressor is calculated using Eq. 40, where h_1 is the compressor inlet enthalpy known from the evaporator outlet conditions and h_{2isen} is the isentropic enthalpy at the compressor outlet.

$$W_{isen} = \dot{m}_r (h_{2isen} - h_1) \tag{40}$$

The isentropic efficiency (η_{isen}) of the compressor depends upon compression ratio defined as the ratio of compressor outlet pressure (P_2) to inlet pressure (P_1). The isentropic efficiency is calculated using a correlation developed by Ortiz et al. [126] for a semi-hematic compressor (Eq. 41).

$$\eta_{isen} = -0.26 + 0.7952 \left(\frac{P_2}{P_1}\right) - 0.2803 \left(\frac{P_2}{P_1}\right)^2 + 0.0414 \left(\frac{P_2}{P_1}\right)^3 \tag{41}$$
$$- 0.0022 \left(\frac{P_2}{P_1}\right)^4$$

5.2.3. Gas Cooler

The gas cooler is modeled as a counter flow concentric tube heat exchanger (Figure 5.2) in which heat is transferred from the supercritical refrigerant to cold water through sensible cooling of the refrigerant. The gas cooler is sized to supply domestic hot water (> 55 °C) for a four membered single-family house in Fargo, North Dakota at a rate of 40 liters/person/day [108]. It has a length of 35 m. The inner tube and outer tube inner diameters are 4.8 mm and 13.48 mm, respectively. The gas cooler outer tube is insulated to prevent any heat loss through it. Table 5.1 presents the specifications of the gas cooler.

Table 5.1: Specifications of the gas cooler.

Components	Parameters	Symbol	Dimension
Gas cooler	Inner tube inner diameter	d_i	4.8 mm
	Inner tube outer diameter	d_o	6.8 mm
	Outer tube inner diameter	D_i	13.48 mm
	Length	L	35 m

In addition to the water inlet temperature, the gas cooler inlet properties of the refrigerant such as temperature, pressure, and enthalpy are known from the compressor outlet. To calculate the gas cooler outlet conditions, the energy balance equations of the refrigerant and water coupled with the conservation equations of the refrigerant are solved.
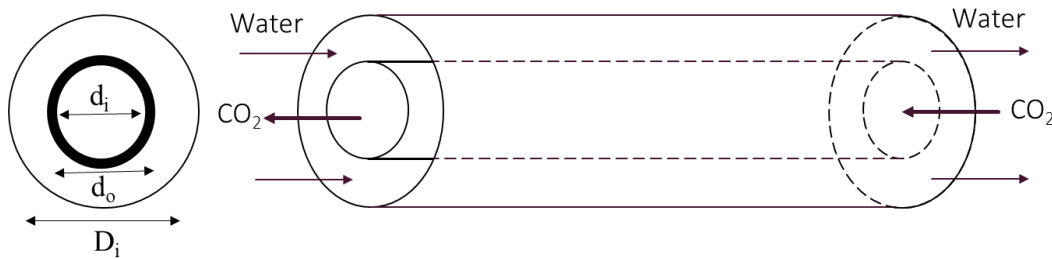
Figure 5.2: Schematic diagram of the gas cooler

The energy balance equation relating the heat transfer from the refrigerant to the water is given in Eq. 42. In Eq. 42, α_s and α_w are refrigerant supercritical HTC and water HTC. Equation 42 couples the individual energy balance equations of the refrigerant (Eq. 47) and the water (Eq. 50). The energy balance (Eq. 42) assumes no conduction resistance through the refrigerant tube wall. Thus, the internal pipe wall temperature, T_p, is the same on both sides of the equation at any given longitudinal location. Equation 42 also assumes that the external surface is well-insulated to prevent heat loss to the environment.

$$A_{s,r}\alpha_s(T_r - T_P) = A_{s,w}\alpha_w(T_p - T_w) \tag{42}$$

The governing equations of the refrigerant flow in the gas cooler are derived assuming an incompressible fluid from the general conservations of mass, momentum, and energy [127].

The continuity and momentum equations of the supercritical refrigerant are shown in Eq. 43 and 44, respectively.

$$\frac{\partial \dot{m}_r}{\partial z} = 0 \tag{43}$$

$$\frac{\partial P}{\partial z} = -\left(\frac{dP}{dz}\right)_f \tag{44}$$

The momentum equation is based on the assumption that the change in momentum is only due to frictional pressure drop in the gas cooler [128]. The frictional pressure drop, $\left(\frac{\partial P}{\partial z}\right)_f$, of CO_2 is evaluated using Eq. 45. The variable, f, is a Darcy frictional factor calculated using Filonenko equation [129] for a straight tube (Eq. 46).

$$\left(\frac{dP}{dz}\right)_f = -f\frac{\rho_r u^2}{2D_{in}} \tag{45}$$

$$f = [1.82 \, log(Re) - 1.64]^{-2} \tag{46}$$

The energy equation of the refrigerant in the supercritical region is given in Eq. 47 which relates the change in enthalpy of the fluid along the length of the gas cooler to the heat transfer with the water.

$$A_{s,p}G\frac{\partial h}{\partial z} = \alpha_s \pi D_{in}(T_r - T_p) \tag{47}$$

The supercritical HTC of the refrigerant (α_s) is calculated using Eq. 48, where Nu_s and k_s are the Nusselt number and thermal conductivity of the refrigerant, respectively. The supercritical Nusselt number is calculated using a correlation proposed by Saltanov et al. [130], which considers the buoyancy effect of CO_2 in the supercritical region (Eq. 49). In Eq. 49, the thermophysical properties are evaluated at the refrigerant bulk temperature with an adjustment for the temperature gradient using the density of the refrigerant at the wall.

$$\alpha_s = \frac{Nu_s \, k_s}{D_{in}} \tag{48}$$

$$Nu_s = 0.0164 Re_b^{0.823} Pr_b^{0.195} \left(\frac{\rho_{wall}}{\rho_b}\right)^{0.374} \tag{49}$$

The energy balance equation describing the longitudinal change in water temperature is given by Eq. 50, where $\dot{m}_w$ and $C_{p,w}$ are the water mass flow rate and specific heat, respectively. The energy balance equation of the water assumes no heat loss to the surroundings.

$$\dot{m}_w C_{p,w} \frac{\partial T_w}{\partial z} = \pi d_o \alpha_w (T_p - T_w) \tag{50}$$

The water HTC (α_w) is calculated using a correlation proposed by Petukhov et al. [131] (Eq. 51) for annular flow using a Nusselt number correction factor (CF), shown in Eq. 52, where D_h is the hydraulic diameter of the annular tube calculated as shown in Eq. 53.

$$\alpha_w = CF \frac{Nu_w \, k_w}{D_h} \tag{51}$$

$$CF = 0.86 \left(\frac{d_o}{D_i}\right)^{-0.16} \tag{52}$$

$$D_h = D_i - d_o \tag{53}$$

The water Nusselt number (Nu_w) is calculated from a modified Gnielinski [132] correlation proposed by Dang et al. [133] for turbulent flow (Eq. 54).

$$Nu_w = \frac{{}^f/_8 \, (Re_w - 1000)Pr_w}{1.07 + 12.7 \left({}^f/_8\right)^{.5} \left(Pr_w{}^{2/3} - 1\right)} \qquad 3000 \leq Re_w \leq 5 \times 10^6 \tag{54}$$

In Eq. 54, f is calculated using Eq. 46 and Re_w is the Reynolds number (Eq. 55).

$$Re_w = \frac{\rho V D_h}{\mu} \tag{55}$$

5.2.4. Expansion Device

The refrigerant expands from a high pressure to a lower pressure fluid by passing through an adiabatic throttling device. Therefore, the throttling process is an isenthalpic process as shown by Eq. 56, where h_3 and h_4 are the specific enthalpy of the refrigerant at the inlet and outlet of the throttling device, respectively.

$$h_3 = h_4 \tag{56}$$

5.2.5. System Performance and Sensitivity Analysis

In order to evaluate the heat pump system performance, the metrics considered are the system coefficient of performance (COP) which is the ratio of water heat absorption to compressor work (Eq. 57), the amount of heat absorbed by the water (Q_w) (Eq. 58), compressor power consumption (W_c) (Eq. 39), and the water temperature at the gas cooler outlet ($T_{w,o}$). The heat pump COP is directly related to the water heat absorption (Q_w), calculated using Eq. 58 and compressor power consumption (W_c) described in section 5.2.2. The water temperature at the gas

cooler outlet ($T_{w,o}$) for a fixed water inlet temperature ($T_{w,i}$) depends on the water heat absorption (Q_w). Ideally, the system will have a high COP while also producing high quality hot water, i.e. outlet water temperatures in excess of 55 °C.

$$COP = \frac{Q_w}{W_c} \qquad (57)$$

$$Q_w = m_w C_{p,w}\left(T_{w,o} - T_{w,i}\right) \qquad (58)$$

To analyze the relative significance of the independent parameters on the heat pump system performance parameters, a sensitivity analysis was conducted. The higher the absolute value of the sensitivity coefficient (Φ), the more dominant an independent variable is on the system performance parameter. The parameter sensitivity coefficient (Φ) is calculated using the one-at-a-time sensitivity measures described by Hamby [134]. The 'local' sensitivity coefficient ($\frac{\partial Y}{\partial X}$) is calculated by changing an independent variable by a small margin while holding all the other variables at the baseline and quantifying the change in output (dependent variable). The average of these local sensitivity coefficient (from baseline to maximum value of the independent variable) is the parameter sensitivity coefficient (Φ), which is shown in Eq. 61. In Eq. 61, n is the total number of independent variable data points considered; and X denotes values of the dimensionless independent variables calculated using Eq. 59 and Y denotes values of the normalized dimensionless dependent variables calculated using Eq. 60.

$$X = \frac{X_{local} - X_{min}}{X_{max} - X_{min}} \qquad (59)$$

$$Y = \frac{Y_{local}}{Y_{baseline}} \qquad (60)$$

$$\Phi = \frac{1}{n-1}\sum \frac{\partial Y}{\partial X} \qquad (61)$$

For evaluating the heat pump seasonal performance, the daily-average heat pump COP, daily-average water heating time (t_H), and the daily-average gross electrical (E_T) output from the PV panels for each season are considered. These seasonal, daily-average values for COP, water heating, and electrical output are determined by using the ambient conditions (e.g. wind speed, temperature, insolation) averaged over each day in the season to get a single ambient condition that represents the average value for a day in that season. See Chapter 7 for more details on the averaging process. The calculation assumes that system is subjected to these average daily values for the entire day.

The seasonal, daily-average heat pump COP is calculated in the same manner as described in Eq. 57. The daily-average water heating time is calculated based on the maximum water mass flow rate in the gas cooler annulus that can be heated from 8 to 60 °C. The daily-average gross electrical output is calculated using Eq. 62. The average daily gross electrical output is the sum of the gross electrical output during operation of the heat pump, $E_{pv,e}$, and when the heat pump is off, E_{pv}. The electrical output is calculated using Eq. 21. For these average conditions, t_H is time the heat pump must operate to heat the water for a family of four. After the water load has been met, the heat pump is assumed to be turned off and thus the quantity $(t_T - t_H)$ is the amount of time during the average day when the heat pump is not running. t_T denotes the total time in a day that solar insolation is available.

$$E_T = E_{pv,e}t_H + E_{pv}(t_T - t_H)$$ (62)

6. NUMERICAL SIMULATION AND MODEL VALIDATION

6.1. Numerical Simulation

The numerical model of the heat pump system is simulated using a code developed in MATLAB. The thermophysical and transport properties of CO_2 are obtained from REFPROP 9.1. The evaporator and the gas cooler are discretized along the length. The energy balance equations and the refrigerant conservation equations are solved at each discretized location using the finite difference scheme.

The simulation flow chart is shown in Figure 6.1. For a particular simulation, the model takes in the geometric parameters and constants (e.g. Table 4.1, Table 5.1, Ambient Conditions) as inputs along with an initial guess value of compressor discharge pressure (P_2) and water outlet temperature ($T_{w,o}$). The model iteratively solves with multiple-layer iteration loops for the inlet/outlet conditions of the evaporator, compressor and gas cooler. The solution scheme for the evaporator is discussed in Section 4.4. Using the evaporator outlet conditions, the model calculates the compressor outlet parameters. The compressor outlet conditions are used as the gas cooler inlet conditions. In the gas cooler, the model calculates the difference between the calculated water inlet temperature, using the initial guess of the water outlet temperature, and specified water inlet temperature. If the difference is greater than a specified tolerance, the model updates the water outlet temperature ($T_{w,o}$) guess value until the difference is smaller than the specified tolerance. Once the iterative loops for the gas cooler have converged, the model calculates the refrigerant enthalpy difference between the gas cooler outlet and evaporator inlet. This is the outer iterative loop shown in Figure 6.1. If the difference is greater than a specified tolerance, the model updates the compressor discharge pressure (P_2), and reevaluates the compressor and gas cooler parameters as described. When the enthalpy difference becomes smaller than the specified tolerance, the

model is assumed to have converged to the steady state solution. The model then evaluates the

heat pump performance parameters.
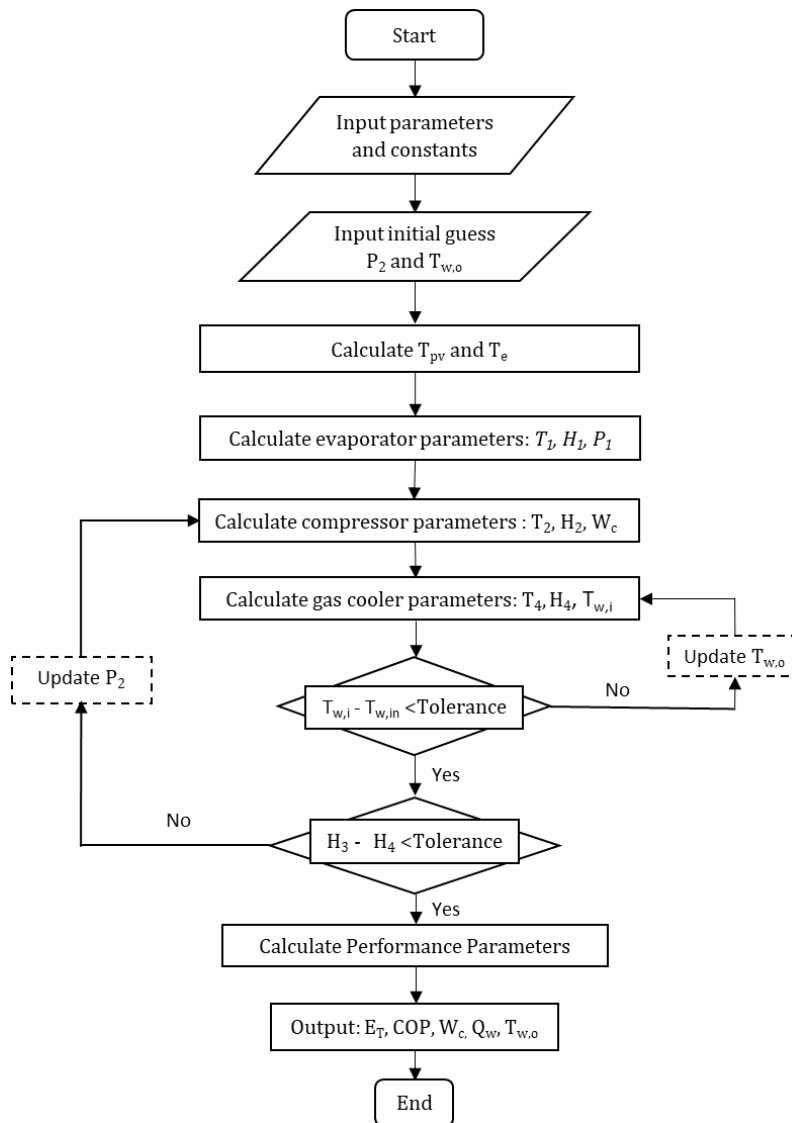
Figure 6.1: Flow chart of the simulation model.

6.2. Model Validation

As discussed in the literature review, a PV/microchannel integrated DXHP with CO_2 as the working fluid has not yet been developed. As such, to validate the model, the two key components: the evaporator and gas cooler, are validated by internal checks and by comparison to experimental data for the isolated component. Chapter 4.3.2 presents the evaporator validation. For the gas cooler, the internal checks include that the mass, momentum, and energy are conserved throughout the gas cooler. Additionally, a mesh refinement study, as shown in Figure 6.2, was completed to ensure there is no discontinuity in the refrigerant properties and that the model is mesh independent. As shown in Figure 6.2, the refrigerant temperature at the gas cooler outlet does not vary significantly for mesh number over 300. This result for refrigerant temperature is consistent with other properties and outputs (e.g. water heat absorption). For subsequent simulations, a mesh number of 400 was used.
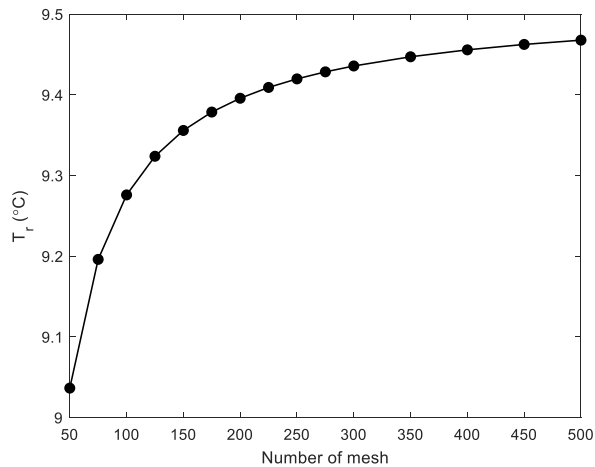
Figure 6.2: Gas cooler mesh study
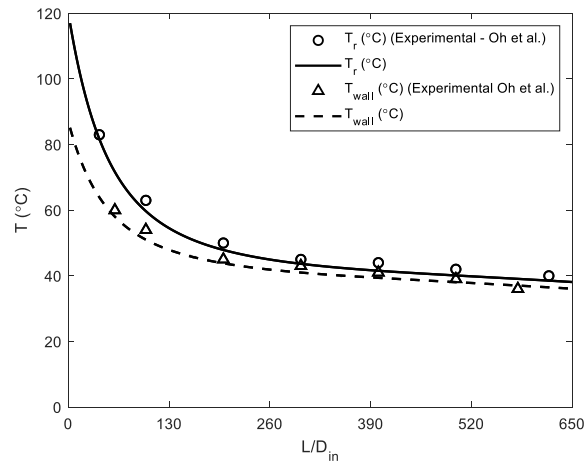
Figure 6.3: Comparison of simulation results with reference studies: CO_2 temperature and wall temperatures of the gas cooler [135].

The external checks include comparing the refrigerant temperature and wall temperature predicted by the model with Oh et al.'s [135] experimental results of supercritical CO_2 gas cooling in a tube-in-tube heat exchanger. Figure 6.3 shows the calculated and experimental refrigerant and wall temperature plotted against dimensionless length. The model predicts the refrigerant temperature within a root mean square deviation (RMSD) of 4.29% and the wall temperature within RMSD of 3.92% compared to the experimental work of Oh et al. [135]. Based on the internal and external checks, it was determined that the model accuracy is enough to investigate the heat pump model.

7. SCOPE OF THE STUDY

To perform a parametric study of the heap pump system, the variables considered are solar insolation, evaporation temperature, refrigerant mass flow rate, and water mass flow rate. Additionally, the effect of ambient temperature is also analyzed in APPENDIX A. Each variable has a baseline value and a range, as summarized in Table 7.1. The simulations run through the range of a variable while holding all the other variables at the baseline values. The baseline solar insolation (500 $W \cdot m^{-2}$) was determined by averaging weather data from NREL typical metrological year 3 (TMY3) [122] between 9 AM to 3 PM from March to October for Fargo, North Dakota. To meet the hot water demand, the heat pump is not required to operate all the hours in a day. As such, the optimal solar insolation available between 9 PM to 3 PM is considered in the present study. The ambient temperature (16 °C) and the wind speed (4.84 $m \cdot s^{-1}$) were determined in the same manner but are held constant for all simulations. The baseline superheating of 5 °C at the evaporator outlet and an evaporation temperature of 0 °C are used in the heat pump study because these conditions are found to be conducive for high heat absorption and reduced pressure drop (Chapter 4). The baseline refrigerant mass flow rate and water mass flow rate are chosen to heat the daily domestic supply water for a family of four (160 liters [108]) from 8 °C , the average city-main-water-supply temperature [136], to >55 °C, which is in the temperature range specified for safe storage of domestic hot water (DHW) [15].

For the sensitivity analysis, a one-at-a-time parameter approach is utilized. The dependent parameter sensitivity for each incremental increase of the independent variable is calculated while all the other variables are held at the baseline value. The sensitivity index for the independent variable is then calculated using Eq. 60.

To evaluate the seasonal heat pump performance, the baseline values of evaporation temperature and CO_2 mass flow rate were kept same as of the parametric study baseline. The water mass flow rate in each season was determined by the rate that would heat 160 liters of water from 8 to 60 °C at a shortest possible time for the given daily-average values. The seasonal solar insolation, ambient temperature, and wind speed were determined by averaging weather data from NREL TMY3 [122] between 9 AM to 3 PM for each day from March to May for spring, June to August for summer, and September to October for fall for Fargo, North Dakota. The seasonal daily-average solar insolation, ambient temperature, and wind speed is presented in Table 7.2.

Table 7.1: Variable parameters ranges and baseline values.

Variables	Ranges	Base Values
Solar insolation	200 to 1000 W·m^{-2}	500 W·m^{-2}
Evaporating temperature	-8 to +7 °C	0 °C
Refrigerant mass flow rate	0.14 to 0.34 kg·s^{-1}	0.021 kg·s^{-1}
Water mass flow rate	0.12 to 0.34 kg·s^{-1}	0.02 kg·s^{-1}

Table 7.2: Seasonal daily-average solar insolation, ambient temperature, and wind speed for Fargo, North Dakota (9 AM to 3 PM).

Season	Solar Insolation (W·m^{-2})	Ambient Temperature (°C)	Wind Speed (m·s^{-1})
Spring	510	10	5.25
Summer	600	23	4.71
Fall	390	14	4.56

8. HEAT PUMP RESULTS AND DISCUSSIONS

8.1. Parametric Study and Sensitivity Analysis

Figure 8.1 shows the effect of solar insolation on the heat pump COP (Figure 8.1a), compressor power consumption (Figure 8.1b), water heat absorption (Figure 8.1c), and outlet water temperature (Figure 8.1d) at evaporation temperatures of -5, 0, and 5 ℃. At a given evaporator temperature, the heat pump COP increases slightly to its maximum value and then decreases slightly with the solar insolation (Figure 8.1a). The reason for this relationship is the competing effects of the higher work input and higher heat transfer with increasing insolation. As the solar insolation increases, the evaporator inlet quality decreases for a fixed evaporator outlet condition. As a result, the compressor discharge pressure increases, which causes the compressor power consumption to increase (Figure 8.1b). At the same time, the heat transfer to the water in the gas cooler also increases (Figure 8.1c) due to an increase in refrigerant temperature at the gas cooler inlet at higher discharge pressure. The heat pump COP increases until the CO_2 temperature at the gas cooler outlet reaches 23 °C. At gas cooler outlet temperatures below 23 °C, the resulting compressor power consumption is high enough to reduce the heat pump COP even though the water heat absorption increases. However, despite the changes in COP, the water outlet temperature increases monotonically with solar insolation (Figure 8.1d) because the heat absorption continues to increase. For example, at the baseline conditions (Evaporator temperature of 0 ℃), the COP is 3.8 at an insolation of 300 $W \cdot m^{-2}$, increases to 4.26 at a solar insolation of 650 $W \cdot m^{-2}$ then decreases to 4.03 at 800 $W \cdot m^{-2}$. The corresponding water outlet temperature increases from 50 to 69.50 to 80 °C. The heat pump performance parameters (COP, compressor power consumption, water heat absorption, and water temperature) follow the same trend for all the evaporator temperatures although the maximum COP increases and shifts to higher solar insolation

values for higher evaporation temperatures, and the outlet water temperature is lower for a higher evaporator temperature at a given insolation level.

Figure 8.1: Effect of solar insolation on the (a) heat pump COP, (b) compressor power consumption, (c) water heat absorption, (d) water outlet temperature at $m_r = 0.021$ kg·s^{-1} and $m_w = 0.021$ kg·s^{-1}.

Figure 8.2: Effect of CO_2 evaporation temperature on the (a) heat pump COP, (b) compressor power consumption, (c) water heat absorption, and (d) water outlet temperature at $I_T = 500$ W·m^{-2} and $m_w = 0.02$ kg·s^{-1}.

Figure 8.2 shows the effect of the evaporation temperature on the heat pump COP (Figure 8.2a), compressor power consumption (Figure 8.2b), water heat absorption (Figure 8.2c), and outlet water temperature (Figure 8.2d) at various CO_2 mass flow rates. For a given refrigerant mass flow rate, the heat pump COP increases with an increase in evaporation temperature (Figure 8.2a), because increasing evaporation temperature causes the evaporator inlet quality to increase for a fixed evaporator outlet condition. As a result, the compressor discharge pressure decreases causing

72

a reduction in compressor power consumption (Figure 8.2b). However, because a lower discharge pressure equates to a lower CO_2 temperature at the gas cooler inlet, there is also a decrease in water heat absorption (Figure 8.2c) and in the outlet water temperature (Figure 8.2d). For example, at a mass flow rate of 0.021 kg·s^{-1} (the baseline condition), increasing evaporation temperature from 0 to 5 °C, slightly increases the COP from 4.16 to 4.29, but the water heat absorption decreases from 4.43 to 3.52 kW and the water outlet temperature decreases from 60.99 to 50.01 °C. This relationship of COP, compressor power consumption, water heat absorption, and water temperature are observed at all refrigerant flow rates, but the increase in COP with evaporation temperature is more pronounced at lower refrigerant flow rates.

Figure 8.3 shows the effect of the CO_2 mass flow rate on the heat pump COP (Figure 8.3a), compressor power consumption (Figure 8.3b), water heat absorption (Figure 8.3c), and outlet water temperature (Figure 8.3d) at various water mass flow rates. Figure 8.3a shows that increasing the CO_2 mass flow rate decreases the heat pump COP because higher refrigerant flow rate requires more compressor work (Figure 8.3b). The heat absorbed by the water also increases with CO_2 flow rate (Figure 8.3c) because of an increase in the refrigerant heat transfer coefficient. However, the outlet water temperature only increases slightly with the refrigerant flow rate (Figure 8.3d) because the CO_2 inlet temperature to the gas cooler is lower at higher flow rates. At higher CO_2 flow rates, the compressor discharge pressure is lower due to an increase in the evaporator-inlet quality for a constant outlet condition. The reduction in discharge pressure reduces CO_2 temperature at the gas cooler inlet. For example, increasing the CO_2 mass flow rate from 0.021 to 0.03 kg·s^{-1} while holding all the other parameters at the baseline conditions, the heat pump COP decreases from 4.12 to 3.14, and the water temperature increases from 60.73 to 64.98 °C. Similar trends for COP, compressor power consumption, water heat absorption, and water temperature are observed at all

73

water mass flow rates, but the increase in outlet water temperature with refrigerant mass flow rate

is more pronounced at lower water mass flow rates.

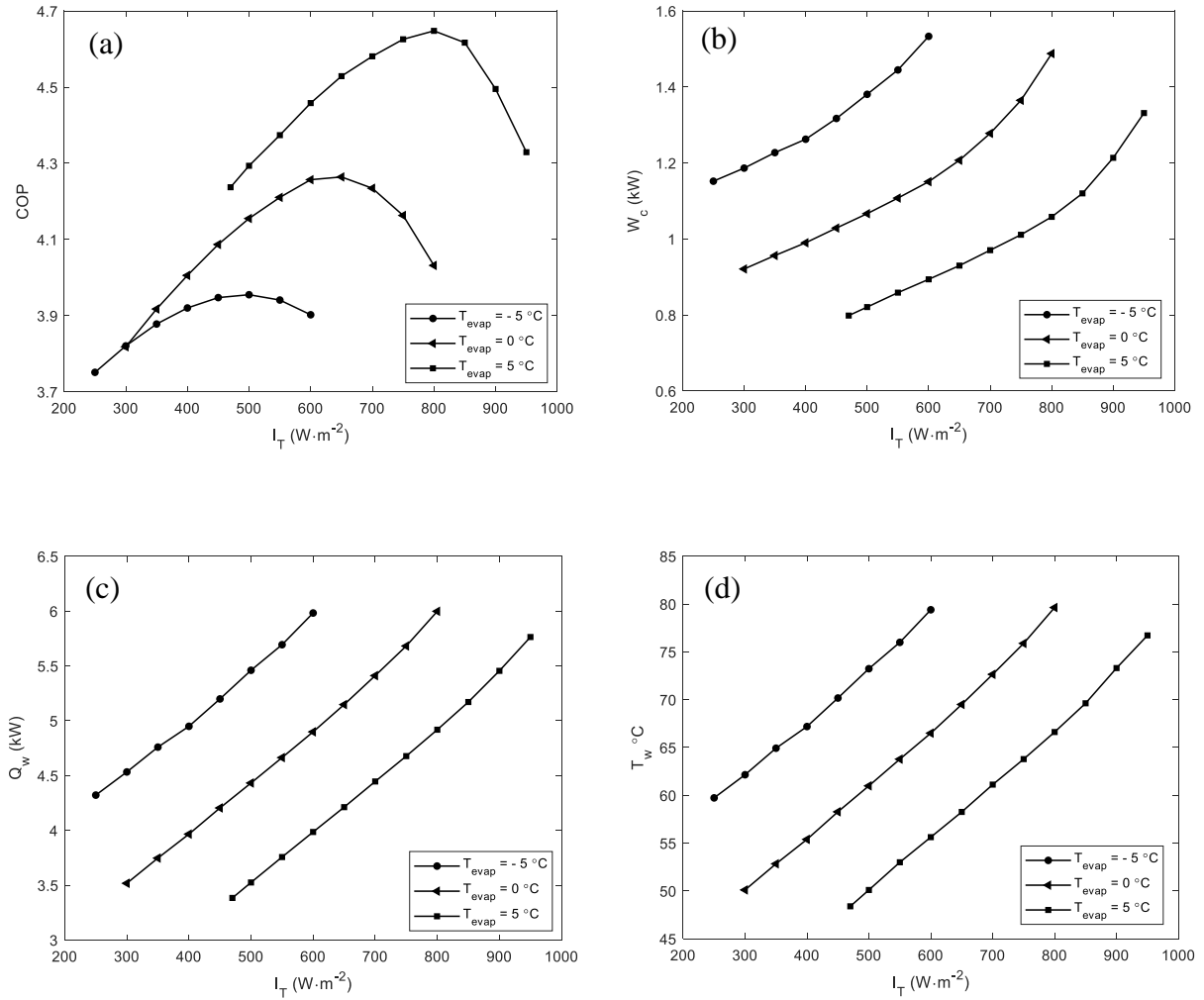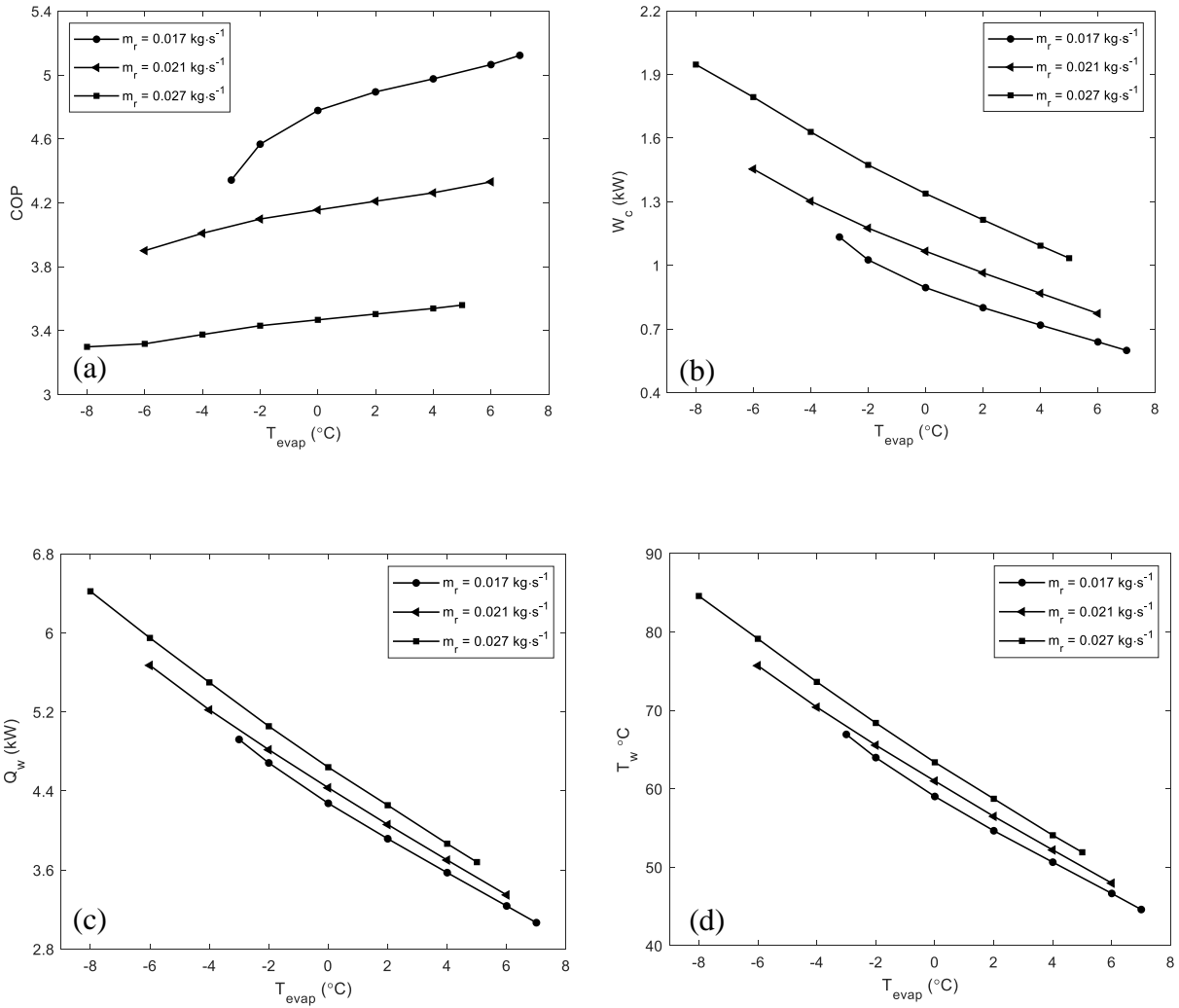Figure 8.3: Effect of CO_2 mass flow rate on the (a) heat pump COP, (b) compressor power consumption, (c) water heat absorption, and (d) water outlet temperature at $I_T = 500$ W·m^{-2} and $T_{evap} = 0$ °C.

Figure 8.4: Effect of water mass flow rate on the (a) heat pump COP, (b) compressor power consumption, (c) water heat absorption, and (d) water outlet temperature at $T_{evap} = 0$ °C and $m_r = 0.021$ kg·s^{-1}.

Figure 8.4 shows the effect of water mass flow rate on the heat pump COP (Figure 8.4a), compressor power consumption (Figure 8.4b), water heat absorption (Figure 8.4c), and outlet water temperature (Figure 8.4d) at various solar insolation. From Figure 8.4a, increasing water mass flow rate increases the heat pump COP. Increasing water mass flow rate reduces compressor discharge pressure and hence, the compressor power consumption (Figure 8.4b). The reduction in discharge pressure causes a reduction in gas cooler inlet CO_2 temperature and consequently, the water heat absorption decreases (Figure 8.4c) even though water mass flow rate increases. As the

75

water heat absorption decreases the water temperature decreases (Figure 8.4d). Increasing water mass flow rate from 0.02 to 0.026 kg·s^{-1} while holding the other operating parameters at the baseline, the heat pump COP increases from 4.16 to 4.49 and the water temperature decreases from 60.99 to 47.84 °C. Similar trend for the COP, compressor power consumption, water heat absorption, and water temperature are observed for all the solar insolation, but higher solar insolation allows the heat pump to heat a higher water mass flow rate.

Summarizing the discussions of Figure 8.1 to Figure 8.4, it was found that increasing solar insolation increases the heat pump COP until the CO_2 temperature at the gas cooler outlet is over 23 °C. The water temperature also increases with the increase in solar insolation. The heat pump COP increases with the increase in evaporation temperature due to reduced required compressor work. However, it also decreases the water temperature. An increased CO_2 mass flow rate decreases the heat pump COP and marginally increases water outlet temperature. Additionally, increasing water mass flow rate increases heat absorption and COP. However, at higher water mass flow rate the water temperature decreases even though the water heat absorption increases.

Figure 8.5 shows the sensitivity analysis of the heat pump COP (Figure 8.5a), compressor power consumption (Figure 8.5b), water heat absorption (Figure 8.5c), and water outlet temperature (Figure 8.5d) at the baseline operating conditions. The higher the absolute value of the sensitivity coefficient of a dependent parameter, the greater the dependency it has on the independent variable. The positive value of the sensitivity coefficient indicates increasing the independent variable value increases the value of the dependent variable and vice versa.
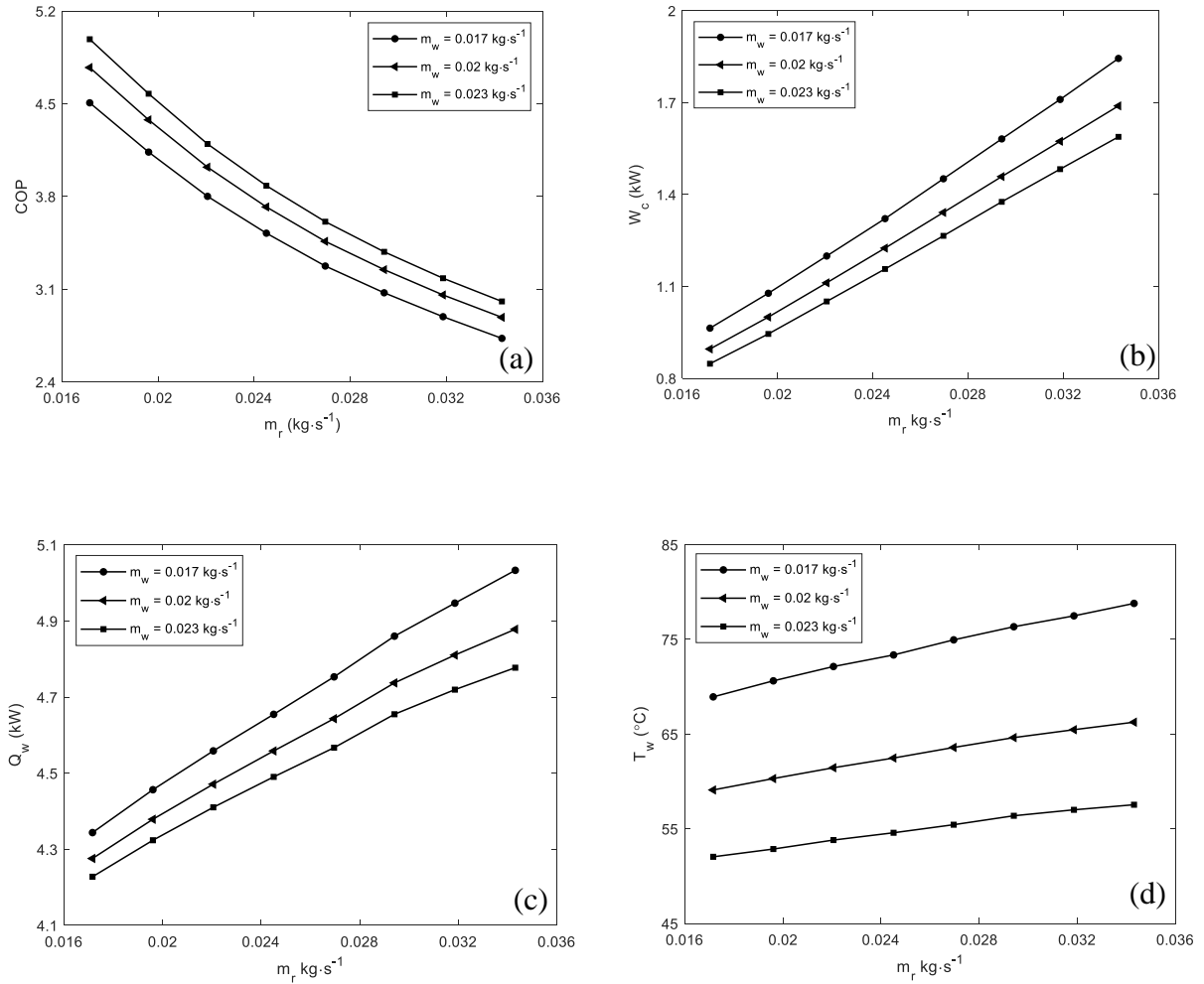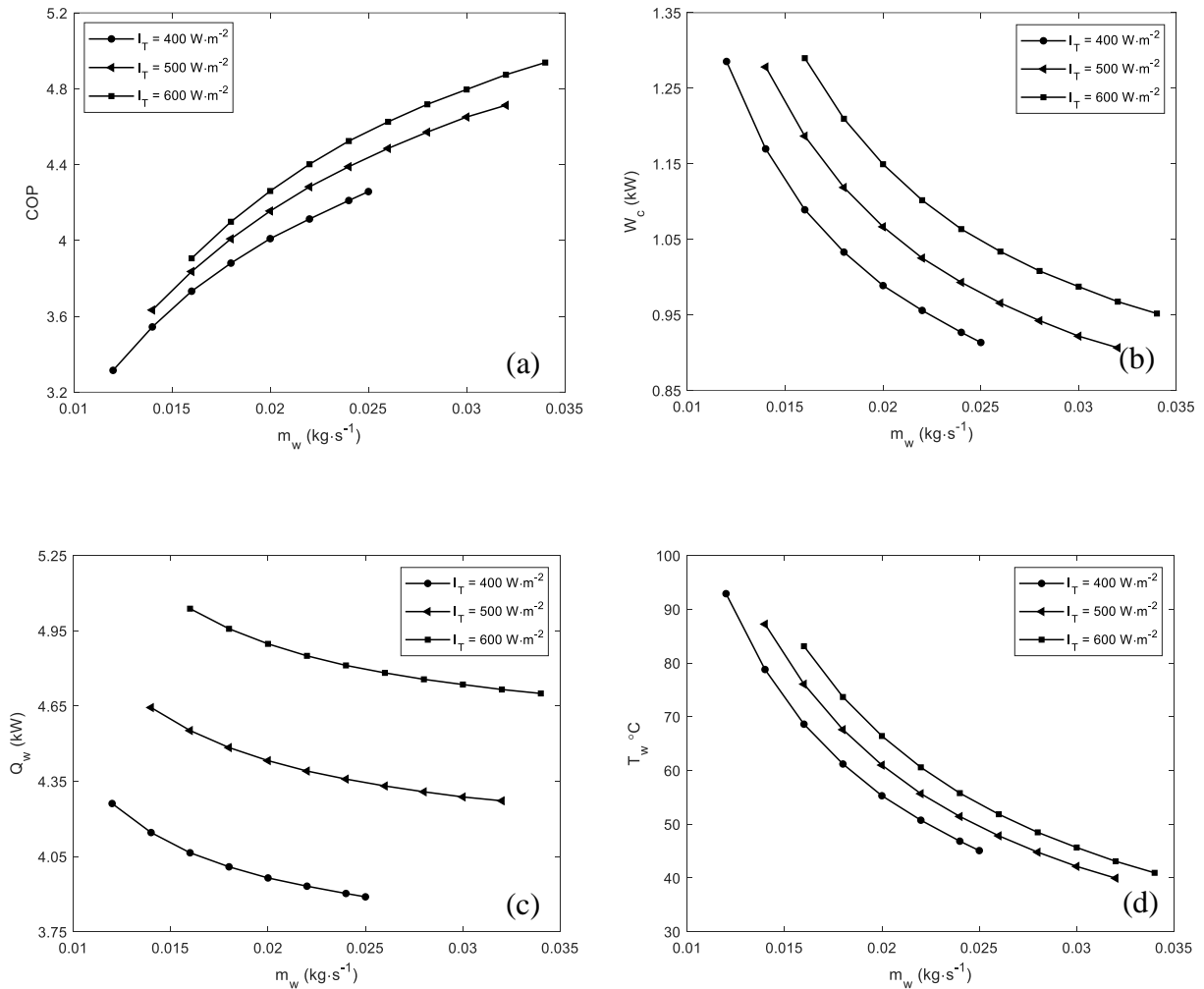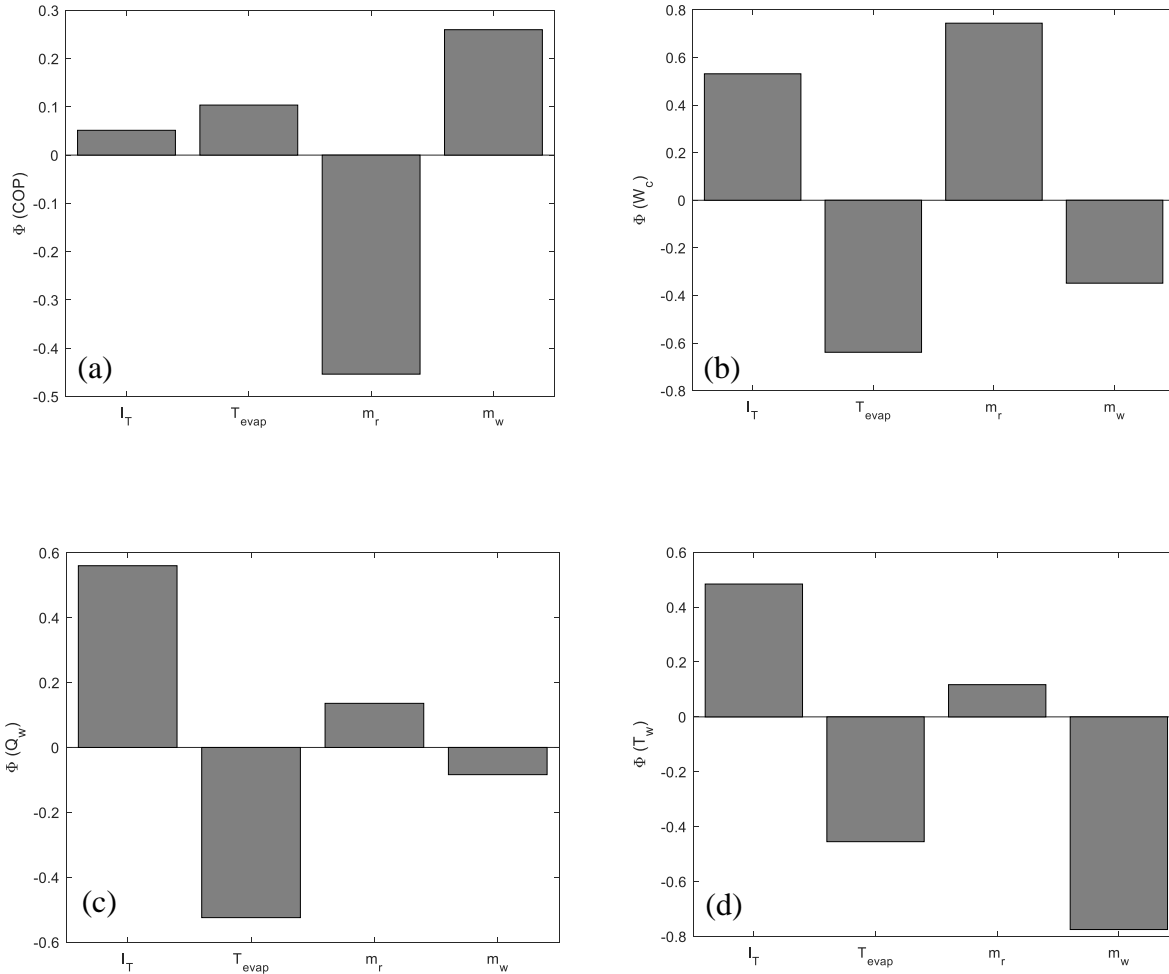
Figure 8.5: Sensitivity analysis of the (a) heat pump COP, (b) compressor power consumption, (c) water heat absorption, and (d) water outlet temperature at the baseline operating conditions.

From Figure 8.5a, the heat pump COP is most sensitive to changes in the CO_2 mass flow rate (-0.45). This sensitivity is primarily due to the high sensitivity of the compressor work to refrigerant flow rate (0.74 – Figure 8.5b). Thus, to maximize the COP, a reduced CO_2 mass flow rate and a higher water mass flow rate is desired. The heat pump COP has the lowest dependency on the solar insolation because of the opposing effect of the high value of compressor power consumption sensitivity coefficient (0.53 – Figure 8.5b) and the water heat absorption sensitivity coefficient (0.56 – Figure 8.5c). From Figure 8.5d, the water outlet temperature is most sensitive

to changes in water mass flow rate (-0.78) followed by evaporation temperature (-0.45). This sensitivity is primarily due to the high sensitivity of the water heat absorption to evaporation temperature (-0.52 – Figure 8.5c). As such operating at a low water mass flow rate and a low evaporation temperature would ensure high water outlet temperature and heat absorption.

8.1.1. Summary of Parametric Study and Sensitivity Analysis

At the baseline operating conditions, the heat pump COP is 4.16 and water outlet temperature is 60 °C. In a study of CO_2 heat pump, Hu et al. [33] found the optimum COP to be 3.29, while heating water to 60 °C. In another study, Saikawa et al. [21] found that the CO_2 heat pump water heater can achieve a COP of 3.0 when heating water from 17 to 65 °C. As such, the PV/microchannel integrated DXHP performs better in comparison, and such performance improvement can be attributed to use of the PV/microchannel evaporator integration.

Additionally, it was found that the PV/microchannel DXHP can achieve a maximum COP of 5.12 and heat water up to 93 °C. There is certainly room to improve the performance over the baseline performance and achieve COP and water temperature close to the maximum by finding the suitable operating conditions. The sensitivity analysis showed that the COP has the highest dependency on the CO_2 mass flow rate. As such, to increase the COP, a low CO_2 mass flow rate is required at the baseline solar insolation (500 Wm^{-2}), evaporation temperature (0 °C), and water mass flow rate (0.02 $kg \cdot s^{-1}$). For example, the heat pump can achieve a COP of 4.77 when the refrigerant mass flow rate is 0.017 $kg \cdot s^{-1}$ while the other operating conditions are kept at the baseline. The water outlet temperature has the highest dependency on the water mass flow rate. To increase the water outlet temperature, a water mass flow rate lower than the baseline is required at the baseline solar insolation (500 Wm^{-2}), evaporation temperature (0 °C), and CO_2 mass flow rate (0.021 $kg \cdot s^{-1}$). For example, the water outlet temperature increases to 76 °C when water mass flow

rate is decreased to 0.016 kg·s^{-1}, while the solar insolation, evaporation temperature, and CO_2 mass flow rate are kept at the baseline.

For the current heat pump geometry, a solar insolation between 500 to 600 W·m^{-2}, commonly encountered in Fargo, ND, an evaporation temperature between 0 to 2 °C, a CO_2 mass flow rate between 0.026 to 0.030 kg·s^{-1}, and water mass flow rate between 0.022 to 0.026 kg·s^{-1} are recommend to maximize the heat pump COP (e.g. 3.8-4.8) while producing hot water constantly over 55 °C.

8.2. Seasonal Performance

Table 8.1 shows the required water mass flow rate for heating 160 liters of water from 8 to 60 °C, daily-average time to heat the water, and the corresponding daily-average COP, compressor power consumption, gross electrical output. For an average day during the summer season, only 1.57 hours is required to heat the water due to the highest required water mass flow rate during the summer. During the fall and spring season required times are 2.62 and 2.70 hours, respectively. Since these times only represent a fraction of the total daylight hours, these results indicate that the system could provide solar fractions of near unity during these seasons. The heat pump has the maximum daily-average COP of 4.10 during the summer season followed by a COP of 3.67 and 3.59 during the fall and spring, respectively. The heat pump daily-average COP is the highest and requires the lowest time to heat the water in the summer because of higher available solar insolation and higher ambient temperature. The daily-average COP and water heating time of the heat pump in spring and fall and are similar even though the available solar insolation during the spring is much higher than fall because of the higher ambient temperature in the fall compared to the spring. The daily-average gross electrical outputs from the PV panels during a 6-hour period (9 AM-3 PM) in a day are 4.40 kWh for spring, 4.83 kWh for summer, and 3.36 kWh for Fall. The heat

79

pump only requires 60.45% of total PV electricity produced during the spring, 49.48% during the summer, and 77.38% of during the fall. These numbers are conservative because only the available radiation from 9 AM to 3 PM is used in the averages. The PV panels could continue to produce electricity outside these times, which would increase the average-daily gross electricity output. Thus, the heat pump does not require any auxiliary electrical input from a source other than the PV panels, and the PV/microchannel integrated CO_2 DXHP is self-sufficient.

Table 8.1: Seasonal performance of the heat pump system and PV electrical output.

Season	Required water mass flow rate $(kg \cdot s^{-1})$	Daily-average time to heat water (Hours)	Daily-average COP	Daily-average compressor power consumption (kWh)	Average-daily gross electrical output (9 AM to 3 PM) (kWh)
Spring	0.0165	2.70	3.59	2.66	4.40
Summer	0.0285	1.57	4.10	2.39	4.83
Fall	0.0170	2.62	3.67	2.60	3.36

The heat pump system was developed primarily for spring, summer, and fall season water heating application with the focus in winter being electricity-only operation. However, the heat pump system could be reconfigured by adding more PV panels and a larger evaporator for all season operation.

9. CONCLUSION AND FUTURE RESEARCH

9.1. Summary and Conclusions

A steady state numerical model of a PV/microchannel integrated DXHP was developed and validated in the present study. A parametric study was performed to understand the effect key operating parameters on its performance, and a sensitivity analysis was performed to analyze relative significance of the operating parameters. Additionally, the heat pump seasonal performance in Fargo, North Dakota weather conditions were analyzed and discussed.

The parametric study showed that the overall performance is not contingent upon one particular parameter independently, rather its performance is dependent on all the parameters concurrently. The sensitivity analysis showed that the COP has the highest sensitivity to the CO_2 mass flow rate followed by the water mass flow rate. The water outlet temperature has high sensitivity to the water mass flow rate followed by the evaporation temperature. While COP and water outlet temperature are both sensitivity to the water mass flow rate, the dependency is reversed. Increasing the water mass flow rate will increase the COP but decrease the water outlet temperature.

In the present study, it was found that the heat pump can achieve a maximum COP of 5.12 and heat water up to 93 °C. Additionally, for the current heat pump configuration and an expected solar insolation between 500 to 600 $W \cdot m^{-2}$, a common value for Fargo, ND, an evaporation temperature between 0 to 2 °C, a CO_2 mass flow rate between 0.026 to 0.030 $kg \cdot s^{-1}$, and water mass flow rate between 0.022 to 0.026 $kg \cdot s^{-1}$ would maximize the heat pump COP (e.g. 3.8-4.8) while producing hot water constantly over 55 °C.

From the seasonal study, it was found that the heat pump has the maximum daily-average COP of 4.10 during the summer season followed by a daily-average COP of 3.67 and 3.59 during

the fall and spring, respectively. During the summer season, at the daily-average values, 1.57 hours is required to heat the 160 liters water from 8 to 60 °C. Additionally, the water heating time during the fall and spring season are very reasonable (~2.5 hours). Based off a conservative 9 AM – 3 PM day, the heat pump uses only 60.45% of total daily-average PV electricity produced during the spring, 49.48% during the summer, and 77.38% of during the fall, which indicates the heat pump is self-sufficient in these seasons.

Overall, the heat pump system incorporates the benefits of the natural refrigerant CO_2, and demonstrates high water heating capability, while maintaining a reasonably high COP, especially for an un-optimized design. The results are highly promising and indicate the system has potential to help meet the energy requirements for residential and industrial water heating demands.

9.2. Future Research

In this study, performance of a PV/microchannel integrated DXHP water heater using CO_2 as the working fluid is analyzed numerically. To ensure the feasibility of such heat pump system more in-depth research both numerical and experimental needs to be carried out. The following recommendations are made for future research:

- ➢ The promising simulation results of the PV/microchannel integrated CO_2 DXHP demands further experimental investigations and validation.

- ➢ Proper sizing of evaporator and gas cooler can contribute to cost cutting while improving the performance of the system. More in depth study needs to be carried out to optimize the heat exchangers sizing for performance improvement.

- ➢ The heat pump cycle modification through integration of an internal heat exchanger, use of multi-stage compression and expansion work recovery device needs to be analyzed for potential performance improvement.

82

➢ This study only focuses on water heating application. However, a heat pump can perform heating and cooling simultaneously. Moreover, such system can be used for space heating as well. Heat pump system that can be used for water and space heating along with summer cooling can be analyzed.

➢ Economic viability of the developed system is not analyzed in the present study. Future study can address the economic viability in terms of cost, life span, and payback period compared to separate PV panels for electricity and solar thermal system for heating application.

REFERENCES

1. EIA (2017) EIA electricity data. In: U.S. Dep. Energy.
    https://www.eia.gov/electricity/monthly/epm_table_grapher.php?t=epmt_es1b. Accessed
    30 Mar 2019

2. Solar Industry Research Data | SEIA. https://www.seia.org/solar-industry-research-data.
    Accessed 30 Mar 2019

3. Dai N, Xu X, Li S, et al (2017) Simulation of Hybrid Photovoltaic Solar Assisted Loop
    Heat Pipe/Heat Pump System. Appl Sci 7:197. https://doi.org/10.3390/app7020197

4. Kong X, Li Y, Lin L, Yang YG (2017) Modeling evaluation of a direct-expansion solar-
    assisted heat pump water heater using R410A. Int J Refrig 76:136–146.
    https://doi.org/10.1016/j.ijrefrig.2017.01.020

5. Chen H, Riffat SB, Fu Y (2011) Experimental study on a hybrid photovoltaic/heat pump
    system. Appl Therm Eng 31:4132–4138.
    https://doi.org/10.1016/J.APPLTHERMALENG.2011.08.027

6. Calise F, Dentice d'Accadia M, Figaj RD, Vanoli L (2016) A novel solar-assisted heat
    pump driven by photovoltaic/thermal collectors: Dynamic simulation and
    thermoeconomic optimization. Energy 95:346–366.
    https://doi.org/10.1016/J.ENERGY.2015.11.071

7. Huang W, Ji J, Xu N, Li G (2016) Frosting characteristics and heating performance of a
    direct-expansion solar-assisted heat pump for space heating under frosting conditions.
    Appl Energy. https://doi.org/10.1016/j.apenergy.2016.03.048

8. Rony RU, Hasan N, Ashiqur M, Laskar R (2018) Heat Transfer of Pulsating Turbulent
    Flow in Pipes. Eur J Adv Eng Technol 5:511–516

9.   Purohit N, Khangarot BS, Gullo P, et al (2017) Assessment of Alumina Nanofluid as a

      Coolant in Double Pipe Gas Cooler for Trans-critical CO2 Refrigeration Cycle. In: Energy

      Procedia. pp 219–226

10.   Reis MNE, Hanriot S (2017) Incompressible pulsating flow for low Reynolds numbers in

      orifice plates. Flow Meas Instrum 54:146–157.

      https://doi.org/10.1016/j.flowmeasinst.2017.01.001

11.   Rony RU, Sumathy K, Gong J (2017) Performance Optimization of a Direct-Expansion

      Solar-Assisted Heat Pump System Employing the PV/Oblique-Finned Micro-channels

      Evaporator Modules. In: ICRSE. Coimbatore, India

12.   Dehghan M, Daneshipour M, Valipour MS, et al (2015) Enhancing heat transfer in

      microchannel heat sinks using converging flow passages. Energy Convers Manag 92:244–

      250. https://doi.org/10.1016/j.enconman.2014.12.063

13.   Yun R, Kim Y, Park C (2007) Numerical analysis on a microchannel evaporator designed

      for CO2 air-conditioning systems. Appl Therm Eng 27:1320–1326.

      https://doi.org/10.1016/j.applthermaleng.2006.10.036

14.   Zhou J, Zhao X, Ma X, et al (2016) Experimental investigation of a solar driven direct-

      expansion heat pump system employing the novel PV/micro-channels-evaporator

      modules. Appl Energy 178:484–495. https://doi.org/10.1016/j.apenergy.2016.06.063

15.   Hang Y, Qu M, Zhao F (2012) Economic and environmental life cycle analysis of solar

      hot water systems in the United States. Energy Build 45:181–188.

      https://doi.org/10.1016/j.enbuild.2011.10.057

16.   Tamura T, Yakumaru Y, Nishiwaki F (2005) Experimental study on automotive cooling

      and heating air conditioning system using CO2 as a refrigerant. Int J Refrig 28:1302–

1307. https://doi.org/10.1016/j.ijrefrig.2005.09.010

17. Rony RU, Yang H, Krishnan S, Song J (2019) Recent advances in transcritical CO 2 (R744) heat pump system: A review. Energies 12:457. https://doi.org/10.3390/en12030457

18. Yamaguchi S, Kato D, Saito K, Kawai S (2011) Development and validation of static simulation model for CO2 heat pump. Int J Heat Mass Transf 54:1896–1906. https://doi.org/10.1016/j.ijheatmasstransfer.2011.01.013

19. Nawaz K, Shen B, Elatar A, et al (2018) Étude de l'influence de la friction sur la performance d'un éjecteur supersonique. Int J Refrig 85:213–228. https://doi.org/10.1016/j.ijrefrig.2017.09.027

20. Environmental Protection Agency U, Star E (2017) ENERGY STAR ®. The simple choice for energy efficiency

21. Saikawa M, Koyama S (2016) Thermodynamic analysis of vapor compression heat pump cycle for tap water heating and development of CO2 heat pump water heater for residential use. Appl Therm Eng 106:1236–1243. https://doi.org/10.1016/j.applthermaleng.2016.06.105

22. Klöcker K, Schmidt EL, Steimle F (2001) Carbon dioxide as a working fluid in drying heat pumps. Int J Refrig 24:100–107. https://doi.org/10.1016/S0140-7007(00)00067-0

23. Schmidtt EL, Kliicker K, Flacke N, Steimle F (1998) PIhS0140-7007(98)00021-8 Applying the transcritical CO2 process to a drying heat pump*. IntJ Refrig 21:202–21

24. Wang D, Yu B, Hu J, et al (2017) Heating performance characteristics of CO 2 heat pump system for electrical vehicle in a cold climate. Int J Refrig 85:27–41. https://doi.org/10.1016/j.ijrefrig.2017.09.009

25. Hakkaki-Fard A, Aidoun Z, Ouzzane M (2014) Applying refrigerant mixtures with thermal glide in cold climate air-source heat pumps. Appl Therm Eng 62:714–722. https://doi.org/10.1016/j.applthermaleng.2013.10.033

26. Hakkaki-Fard A, Aidoun Z, Ouzzane M (2015) Improving cold climate air-source heat pump performance with refrigerant mixtures. Appl Therm Eng 78:695–703. https://doi.org/10.1016/j.applthermaleng.2014.11.036

27. Potential development of air source Heat Pump in the UK. http://www.esru.strath.ac.uk/EandE/Web_sites/10-11/ASHP_CO2/lit-sanyoEcoCute.html. Accessed 9 Jun 2019

28. Sanden CO2 Heat Pump Water Heater - SanCO2 - Sanden. https://www.sandenwaterheater.com/. Accessed 9 Jun 2019

29. Tian H, Yang Z, Li M, Ma Y (2009) Research and application of CO 2 refrigeration and heat pump cycle. Sci China, Ser E Technol Sci 52:1563–1575. https://doi.org/10.1007/s11431-009-0175-4

30. Austin BT, Sumathy K (2011) Transcritical carbon dioxide heat pump systems: A review. Renew. Sustain. Energy Rev.

31. Hu B, Wang X, Cao F, et al (2014) Experimental analysis of an air-source transcritical CO2 heat pump water heater using the hot gas bypass defrosting method. Appl Therm Eng 71:528–535. https://doi.org/10.1016/j.applthermaleng.2014.07.017

32. Calabrese N, Mastrullo R, Mauro AW, et al (2015) Performance analysis of a rooftop, air-to-air heat pump working with CO2. Appl Therm Eng 75:1046–1054. https://doi.org/10.1016/j.applthermaleng.2014.10.057

33. Hu B, Li Y, Cao F, Xing Z (2015) Extremum seeking control of COP optimization for air-

source transcritical CO2 heat pump water heater system. Appl Energy 147:361–372. https://doi.org/10.1016/j.apenergy.2015.03.010

34.   Hu B, Li Y, Wang R, et al (2017) Real-time minimization of power consumption for air-source transcritical CO 2 heat pump water heater system. Int J Refrig 85:395–408. https://doi.org/10.1016/j.ijrefrig.2017.10.016

35.   Liu F, Zhu W, Cai Y (2017) Experimental Study of a Dual-mode CO2 Heat Pump System with Thermal Storage. In: Energy Procedia. pp 4078–4083

36.   Murray P, Harrison S, Johnson G, Stinson B (2014) Experimental Evaluation of a Water Source CO2 Heat Pump Incorporating Novel Gas-Cooler Configuration. V002T12A004. https://doi.org/10.1115/es2014-6668

37.   Jinggang W, Ligai K, Jie L (2009) CO2 transcritical cycle for ground source heat pump. In: 2009 WRI World Congress on Computer Science and Information Engineering, CSIE 2009. pp 213–217

38.   Eslami-Nejad P, Ouzzane M, Aidoun Z (2014) Modeling of a two-phase CO2-filled vertical borehole for geothermal heat pump applications. Appl Energy 114:611–620. https://doi.org/10.1016/j.apenergy.2013.10.028

39.   Deng S, Dai YJ, Wang RZ (2012) Performance study on hybrid solar-assisted CO 2 heat pump system based on the energy balance of net zero energy apartment. Energy Build 54:337–349. https://doi.org/10.1016/j.enbuild.2012.08.009

40.   Deng S, Dai YJ, Wang RZ, et al (2011) Comparison study on performance of a hybrid solar-assisted CO2 heat pump. In: Applied Thermal Engineering. pp 3696–3705

41.   Emmi G, Zarrella A, De Carli M, Galgaro A (2015) Solar assisted ground source heat pump in cold climates. In: Energy Procedia. pp 623–629

42. Chen JF, Dai YJ, Wang RZ (2016) Experimental and theoretical study on a solar assisted CO_2 heat pump for space heating. Renew Energy 89:295–304. https://doi.org/10.1016/j.renene.2015.12.039

43. Faria RN, Nunes RO, Koury RNN, Machado L (2016) Dynamic modeling study for a solar evaporator with expansion valve assembly of a transcritical CO_2heat pump. Int J Refrig 64:203–213. https://doi.org/10.1016/j.ijrefrig.2016.01.004

44. Raisul Islam M, Sumathy K, Gong J, Ullah Khan S (2017) Performance study on solar assisted heat pump water heater using CO_2 in a transcritical cycle. Renew Energy Power Qual J 1421–1425. https://doi.org/10.24084/repqj10.720

45. Li S, Li S, Zhang X (2015) Simulation research of a hybrid heat source heat pump using R134a, R744 instead of R22 for domestic water heating in residential buildings. Energy Build 91:57–64. https://doi.org/10.1016/j.enbuild.2015.01.019

46. Cho H (2015) Comparative study on the performance and exergy efficiency of a solar hybrid heat pump using R22 and R744. Energy 93:1267–1276. https://doi.org/10.1016/j.energy.2015.10.016

47. Jin Z, Eikevik TM, Nekså P, Hafner A (2017) A steady and quasi-steady state analysis on the CO_2 hybrid ground-coupled heat pumping system. Int J Refrig 76:29–41. https://doi.org/10.1016/j.ijrefrig.2017.01.029

48. Jin Z, Eikevik TM, Nekså P, Hafner A (2016) Investigation on CO_2 hybrid ground-coupled heat pumping system under warm climate. Int J Refrig 62:145–152. https://doi.org/10.1016/j.ijrefrig.2015.10.005

49. Kim W, Choi J, Cho H (2013) Performance analysis of hybrid solar-geothermal CO_2 heat pump system for residential heating. Renew Energy 50:596–604.

https://doi.org/10.1016/j.renene.2012.07.020

50. Thome JR, Ribatski G (2005) State-of-the-art of two-phase flow and flow boiling heat transfer and pressure drop of CO2 in macro- and micro-channels. Int. J. Refrig. 28:1149–1168

51. Pettersen J, Hafner A, Skaugen G, Rekstad H (1998) Development of compact heat exchangers for CO2 air-conditioning systems. Int J Refrig 21:180–193. https://doi.org/10.1016/S0140-7007(98)00013-9

52. Thome JR, Ribatski G (2005) State-of-the-art of two-phase flow and flow boiling heat transfer and pressure drop of CO2 in macro- and micro-channels. Int. J. Refrig. 28:1149–1168

53. Kwang-Il Choi, Pamitran A, Jong-Taek Oh (2007) Two-phase flow heat transfer of CO2 vaporization in smooth horizontal minichannels. Int J Refrig 30:. https://doi.org/10.1016/j.ijrefrig.2006.12.006

54. Oh J, Pamitran AS, Choi K, Hrnjak P (2011) International Journal of Heat and Mass Transfer Experimental investigation on two-phase flow boiling heat transfer of five refrigerants in horizontal small tubes of 0 . 5 , 1 . 5 and 3 . 0 mm inner diameters. Int J Heat Mass Transf 54:2080–2088. https://doi.org/10.1016/j.ijheatmasstransfer.2010.12.021

55. Bremer J, Wu J, Koettig T, et al (2011) Investigation of heat transfer and pressure drop of CO(2) two-phase flow in a horizontal minichannel. Int J Heat Mass Transf 54:2154–2162. https://doi.org/10.1016/j.ijheatmasstransfer.2010.12.009

56. Yun R, Kim Y, Soo Kim M, Choi Y (2003) Boiling heat transfer and dryout phenomenon of CO 2 in a horizontal smooth tube. Int J Heat Mass Transf 46:2353–2361. https://doi.org/10.1016/S0017-9310(02)00540-9

57. Cheng L, Ribatski G, Moreno Quibén J, Thome JR (2008) New prediction methods for CO2 evaporation inside tubes: Part I – A two-phase flow pattern map and a flow pattern based phenomenological model for two-phase flow frictional pressure drops. Int J Heat Mass Transf 51:111–124. https://doi.org/10.1016/j.ijheatmasstransfer.2007.04.002

58. Yun R, Kim Y, Park C (2007) Numerical analysis on a microchannel evaporator designed for CO2 air-conditioning systems. Appl Therm Eng 27:1320–1326. https://doi.org/10.1016/j.applthermaleng.2006.10.036

59. Bendaoud A, Ouzzane M, Aidoun Z, Galanis N (2010) A new modeling approach for the study of finned coils with CO2. Int J Therm Sci 49:1702–1711. https://doi.org/10.1016/j.ijthermalsci.2010.04.002

60. Yoon SH, Cho ES, Hwang YW, et al (2004) Characteristics of evaporative heat transfer and pressure drop of carbon dioxide and correlation development. In: International Journal of Refrigeration. pp 111–119

61. Bredesen AM, Hafner A, Pettersen J, et al (1997) Heat transfer and pressure drop for in-tube evaporation of CO2. In: International Conference on Heat Transfer Issues in Natural Refrigerants. pp 35–49

62. Knudsen HJH, Jensen PH (1998) Heat transfer coefficient for boiling carbon dioxide. Compression Syst With Nat Work Fluids 319–328

63. Jiang Y, Ma Y, Li M, Fu L (2013) An experimental study of trans-critical CO2 water-water heat pump using compact tube-in-tube heat exchangers. Energy Convers Manag 76:92–100. https://doi.org/10.1016/j.enconman.2013.07.031

64. Sato H, Kimata Y, Hotta Y, et al (2012) Development of Two-Stage Compressor for CO2 Heat-Pump Water Heaters. Mitsubishi Heavy Ind Tech Rev 49:92–97

65. Hiwata A, Iida N, Futagami Y, et al (2002) Performance Investigation With Oil-Injection to Compression Chambers On CO2-Scroll Compressor. In: International Compressor Engineering Conference. p 8

66. Shimoji M, Adv TN-ME, 2007 U Performance analysis of scroll compressors using CO2 refrigerant. mitsubishielectric.com

67. Rozhentsev A, Wang C-C (2001) Some design features of a CO$_2$air conditioner. Appl Therm Eng 21:. https://doi.org/10.1016/S1359-4311(00)00087-9

68. Cavallini A, Cecchinato L, Corradi M, et al (2005) Two-stage transcritical carbon dioxide cycle optimisation: A theoretical and experimental analysis. Int J Refrig 28:1274–1283. https://doi.org/10.1016/j.ijrefrig.2005.09.004

69. Zhang L, Yang M, Huang X (2016) Performance Comparison of Single-stage and Two-stage Hermetic Rotary CO2 Compressor

70. Pitarch M, Navarro-Peris E, Gonzalvez J, Corberan JM (2015) Analysis and optimisation of different two-stage transcritical carbon dioxide cycles for heating applications. Int J Refrig 70:235–242. https://doi.org/10.1016/j.ijrefrig.2015.08.013

71. Xing M, Yu J, Liu X (2014) Thermodynamic analysis on a two-stage transcritical CO2 heat pump cycle with double ejectors. Energy Convers Manag 88:677–683. https://doi.org/10.1016/j.enconman.2014.09.025

72. Liu S, Sun Z, Li H, et al (2017) Thermodynamic analysis of CO2 transcritical two-stage compression refrigeration cycle systems with expanders. HKIE Trans Hong Kong Inst Eng 24:70–77. https://doi.org/10.1080/1023697X.2017.1314198

73. Chang YS, Kim MS (2007) Modeling and performance simulation of a gas cooler for a co2 Heat Pump System. HVAC R Res 13:445–456.

https://doi.org/10.1080/10789669.2007.10390964

74. Liao SM, Zhao TS (2002) An experimental investigation of convection heat transfer to supercritical carbon dioxide in miniature tubes. Int J Heat Mass Transf 45:5025–5034. https://doi.org/10.1016/S0017-9310(02)00206-5

75. Dang C, Hihara E (2004) In-tube cooling heat transfer of supercritical carbon dioxide. Part 1. Experimental measurement. Int J Refrig 27:736–747. https://doi.org/10.1016/j.ijrefrig.2004.04.018

76. Wang Q, Chen Y, Xu X, et al (2015) An experimental study on heat transfer between supercritical carbon dioxide and water near the pseudo-critical temperature in a double pipe heat exchanger. Int J Heat Mass Transf 93:379–387. https://doi.org/10.1016/j.ijheatmasstransfer.2015.10.017

77. Du Z, Lin W, Gu A (2010) Numerical investigation of cooling heat transfer to supercritical CO_2 in a horizontal circular tube. J Supercrit Fluids 55:116–121. https://doi.org/10.1016/j.supflu.2010.05.023

78. Naphon P, Wongwises S (2006) A review of flow and heat transfer characteristics in curved tubes. Renew. Sustain. Energy Rev. 10:463–490

79. Yang D, Xie J, Lv J, Wang J (2017) An experimental and numerical study of helix tube gas cooler for super-critical carbon dioxide. J Chem Eng Japan 50:900–908. https://doi.org/10.1252/jcej.17we018

80. J.D. Jackson, M.A. Cotton, B.P. Axcell (1989) Studies of mixed convection in vertical tubes. Int J Heat Fluid Flow 10:2–15. https://doi.org/10.1016/0142-727X(89)90049-0

81. Forooghi P, Hooman K (2013) Numerical study of turbulent convection in inclined pipes with significant buoyancy influence. Int J Heat Mass Transf 61:310–322.

https://doi.org/10.1016/j.ijheatmasstransfer.2013.02.014

82. Santosa IdMC, Gowreesunker BL, Tassou SA, et al (2017) Investigations into air and refrigerant side heat transfer coefficients of finned-tube CO2 gas coolers. Int J Heat Mass Transf 107:168–180. https://doi.org/10.1016/j.ijheatmasstransfer.2016.11.011

83. Li J, Jia J, Huang L, Wang S (2017) Experimental and numerical study of an integrated fin and micro-channel gas cooler for a CO 2 automotive air-conditioning. Appl Therm Eng 116:636–647. https://doi.org/10.1016/j.applthermaleng.2016.12.140

84. Garimella S, Bansal PK (2002) Microchannel gas coolers for carbon dioxide air-conditioning systems. In: ASHRAE Transactions. pp 492–499

85. Chang YS, Kim MS (2007) Modeling and performance simulation of a gas cooler for a co2 Heat Pump System. HVAC R Res 13:445–456. https://doi.org/10.1080/10789669.2007.10390964

86. Yingying Y, Minxia L, Kaiyang W, Yitai M (2016) Study of multi-twisted-tube gas cooler for CO 2 heat pump water heaters. Appl Therm Eng 102:204–212. https://doi.org/10.1016/j.applthermaleng.2016.03.123

87. Kim YJ, Chang KS (2013) Development of a thermodynamic performance-analysis program for CO2 geothermal heat pump system. J Ind Eng Chem 19:1827–1837. https://doi.org/10.1016/j.jiec.2013.02.028

88. Marcinichen JB, Thome JR, Pereira RH (2016) Working fluid charge reduction. Part II: Supercritical CO2 gas cooler designed for light commercial appliances. Int J Refrig 65:273–286. https://doi.org/10.1016/j.ijrefrig.2015.12.018

89. Chen Y-G (2016) Pinch point analysis and design considerations of CO2 gas cooler for heat pump water heaters. Int J Refrig 69:136–146.

https://doi.org/10.1016/j.ijrefrig.2016.05.003

90. Cabello R, Llopis R, Torrella E (2012) Development and validation of a finite element model for water – CO 2 coaxial. Methodology 93:637–647. https://doi.org/10.1016/j.apenergy.2011.12.100

91. Yin JM, Bullard CW, Hrnjak PS (2001) R-744 gas cooler model development and validation. Int J Refrig 24:692–701. https://doi.org/10.1016/S0140-7007(00)00082-7

92. Liu F, Zhu W, Zhao J, et al (2017) A new method for optimal control of a dual-mode CO2 heat pump with thermal storage. Appl Therm Eng 125:1123–1132. https://doi.org/10.1016/j.applthermaleng.2017.07.068

93. Hu B, Li Y, Wang RZ, et al (2018) Real-time minimization of power consumption for air-source transcritical CO2 heat pump water heater system. Int J Refrig 85:395–408. https://doi.org/10.1016/j.ijrefrig.2017.10.016

94. Peñarrocha I, Llopis R, Tárrega L, et al (2014) A new approach to optimize the energy efficiency of CO2 transcritical refrigeration plants. Appl Therm Eng 67:137–146. https://doi.org/10.1016/j.applthermaleng.2014.03.004

95. Kim MS, Kang DH, Kim MS, Kim M (2017) Investigation on the optimal control of gas cooler pressure for a CO 2 refrigeration system with an internal heat exchanger. Int J Refrig 77:48–59. https://doi.org/10.1016/j.ijrefrig.2017.03.002

96. Sumeru K, Nasution H, Ani FN (2012) A review on two-phase ejector as an expansion device in vapor compression refrigeration cycle. Renew. Sustain. Energy Rev. 16:4927–4937

97. Elbel S, Hrnjak P (2008) Experimental validation of a prototype ejector designed to reduce throttling losses encountered in transcritical R744 system operation ´ rimentale d '

un e ´jecteur prototype conc Validation expe x u pour ´duire les pertes de laminage lors du fonctionne. Control 31:411–422. https://doi.org/10.1016/j.ijrefrig.2007.07.013

98. Zheng L, Deng J, He Y, Jiang P (2015) Dynamic model of a transcritical CO2 ejector expansion refrigeration system. Int J Refrig 60:247–260. https://doi.org/10.1016/j.ijrefrig.2015.08.019

99. He Y, Deng J, Zhang Z (2014) Thermodynamic study on a new transcritical CO2 ejector expansion refrigeration system with two-stage evaporation and vapor feedback. HVAC R Res 20:655–664. https://doi.org/10.1080/10789669.2014.929422

100. Boccardi G, Botticella F, Lillo G, et al (2016) Thermodynamic Analysis of a Multi-Ejector, CO2, Air-To-Water Heat Pump System. In: Energy Procedia. pp 846–853

101. Smolka J, Palacz M, Bodys J, et al (2016) Performance comparison of fixed- and controllable-geometry ejectors in a CO2 refrigeration system. Int J Refrig 65:172–182. https://doi.org/10.1016/j.ijrefrig.2016.01.025

102. Liu F, Groll EA, Ren J (2016) Comprehensive experimental performance analyses of an ejector expansion transcritical CO2 system. Appl Therm Eng 98:1061–1069. https://doi.org/10.1016/j.applthermaleng.2015.12.017

103. Xiao X, Ming G, Ming L, Jiang Z (2012) Experimental investigation on performance of transcritical CO 2 heat pump system with ejector under optimum high-side pressure. Energy 44:870–877. https://doi.org/10.1016/j.energy.2012.04.062

104. Zhang Z, Dong X, Ren Z, et al (2017) Influence of refrigerant charge amount and EEV opening on the performance of a transcritical CO2 heat pump water heater. Energies 10:. https://doi.org/10.3390/en10101521

105. Baek C, Heo J, Jung J, et al (2013) Optimal control of the gas-cooler pressure of a CO 2

heat pump using EEV opening and outdoor fan speed in the cooling mode. Int J Refrig 36:1276–1284. https://doi.org/10.1016/j.ijrefrig.2013.02.009

106. Song Y, Wang J, Cao F, et al (2017) Experimental investigation on a capillary tube based transcritical CO2 heat pump system. Appl Therm Eng 112:184–189. https://doi.org/10.1016/j.applthermaleng.2016.10.033

107. Madsen KB, Poulsen CS, Wiesenfarth M (2005) Study of capillary tubes in a transcritical CO 2 refrigeration system. Int J Refrig 28:1212–1218. https://doi.org/10.1016/j.ijrefrig.2005.09.009

108. Yurtsev A, Jenkins GP (2016) Cost-effectiveness analysis of alternative water heater systems operating with unreliable water supplies. Renew. Sustain. Energy Rev. 54:174–183

109. Ji J, He H, Chow T, et al (2009) Distributed dynamic modeling and experimental study of PV evaporator in a PV/T solar-assisted heat pump. Int J Heat Mass Transf 52:1365–1373. https://doi.org/10.1016/j.ijheatmasstransfer.2008.08.017

110. Kim MH, Bullard CW (2001) Development of a microchannel evaporator model for a CO 2 air-conditioning system. Energy 26:931–948. https://doi.org/10.1016/S0360-5442(01)00042-1

111. Ducoulombier M, Colasson S, Bonjour J, Haberschill P (2011) Carbon dioxide flow boiling in a single microchannel – Part II: Heat transfer. Exp Therm Fluid Sci 35:597–611. https://doi.org/10.1016/J.EXPTHERMFLUSCI.2010.11.014

112. Premoli A. FD, Prima A (1970) An Empirical Correlation for Evaluating Two-Phase Mixture Density under Adiabatic Conditions. Eur. Two-Phase Flow Gr. Meet. 1970

113. Chisholm D (1973) Pressure gradients due to friction during the flow of evaporating two-

phase mixtures in smooth tubes and channels. Int J Heat Mass Transf 16:347–358. https://doi.org/10.1016/0017-9310(73)90063-X

114. Chisholm D (1967) A theoretical basis for the Lockhart-Martinelli correlation. Appl Heat Transf Div 10:1767–1778. https://doi.org/http://dx.doi.org/10.1016/0017-9310(67)90047-6

115. Yun R, Engineering YK-MT, 2004 U (2004) TWO-PHASE PRESSURE DROP OF CO2 IN MINI TUBES AND MICROCHANNELS. Taylor Fr

116. Lockhart R, Prog RM-CE, 1949 U (1949) Proposed correlation of data for isothermal two-phase, two-component flow in pipes. dns2.asia.edu.tw

117. Chen JC (1966) Correlation for boiling heat transfer to saturated fluids in convective flow. Ind Eng Chem Process Des Dev 5:322–329. https://doi.org/10.1021/i260019a023

118. Kwang-Il Choi, Pamitran A, Jong-Taek Oh (2007) Two-phase flow heat transfer of CO2 vaporization in smooth horizontal minichannels. Int J Refrig 30:. https://doi.org/10.1016/j.ijrefrig.2006.12.006

119. Cooper MG (1984) Heat flow in saturated nucleate pool boiling - a wide-ranging examination using reduced properties. Adv Heat Transf 16:. https://doi.org/10.1016/S0065-2717(08)70205-3

120. Linlin J, Jianhua L, Liang Z, et al (2017) Characteristics of heat transfer for CO 2 flow boiling at low temperature in mini-channel. Int J Heat Mass Transf 108:2120–2129. https://doi.org/10.1016/j.ijheatmasstransfer.2016.12.113

121. Pettersen J (2004) Flow vaporization of CO2 in microchannel tubes. Exp Therm Fluid Sci 28:111–121. https://doi.org/10.1016/S0894-1777(03)00029-3

122. National Renewable Energy Laboratory (NREL) (2018) NSRDB: 1991- 2005 Update:

TMY3. In: Natl. Renew. Energy Lab. https://rredc.nrel.gov/solar/old_data/nsrdb/1991-2005/tmy3/. Accessed 30 Mar 2019

123. Austin BT, Sumathy K (2011) Parametric study on the performance of a direct-expansion geothermal heat pump using carbon dioxide. In: Applied Thermal Engineering. pp 3774–3782

124. Sarkar J, Bhattacharyya S, Gopal MR (2004) Optimization of a transcritical CO2 heat pump cycle for simultaneous cooling and heating applications. Int J Refrig 27:830–838. https://doi.org/10.1016/J.IJREFRIG.2004.03.006

125. Deng J, Jiang P, Lu T, Lu W (2007) Particular characteristics of transcritical CO2 refrigeration cycle with an ejector. Appl Therm Eng 27:381–388. https://doi.org/10.1016/J.APPLTHERMALENG.2006.07.016

126. Oritz T, Li D, Groll E (2003) Evaluation of the performance potential of CO2 as a refrigerant in air-to-air Air conditioners and heat pumps: system modeling and analysis

127. Chen L, Zhang XR, Yamaguchi H, Liu ZS (2010) Effect of heat transfer on the instabilities and transitions of supercritical CO2 flow in a natural circulation loop. Int J Heat Mass Transf 53:4101–4111. https://doi.org/10.1016/j.ijheatmasstransfer.2010.05.030

128. Liu Z, He Y, Yang Y, et al Experimental study on heat transfer and pressure drop of supercritical CO2 cooled in a large tube. Elsevier

129. Fang X, Xu Y, Su X, Shi R (2012) Pressure drop and friction factor correlations of supercritical flow. Nucl Eng Des. https://doi.org/10.1016/j.nucengdes.2011.10.041

130. Saltanov E, Pioro I, Harvel G (2015) ICONE23-2018 INNOVATIVE APPROACH TO CORRELATE HEAT-TRANSFER DATA TO SUPECRITICAL CARBON DIOXIDE FLOWING UPWARD IN A BARE TUBE. Proc Int Conf Nucl Eng 2015.23:_ICONE23-

2-_ICONE23-2. https://doi.org/10.1299/jsmeicone.2015.23._ICONE23-2_8

131. Petukhov BS, Roizen LI (1964) Generalized relationships for heat transfer in a turbulent

flow of gas in tubes of annular section(Heat transfer coefficients and adiabatic

temperatures obtained for turbulent gas flow in tubes with annular section). High Temp

2:65–68

132. Gnielinski V (1976) New equations for heat and mass transfer in turbulent pipe and

channel flow. Int Chem Eng

133. Dang C, Hihara E (2004) In-tube cooling heat transfer of supercritical carbon dioxide. Part

1. Experimental measurement. In: International Journal of Refrigeration

134. D. M. Hamby (1994) A Review of Techniques for Parameter Sensitivity Analysis of

Environmental Models. Environ Monit Assess 32:135–154.

https://doi.org/10.1007/BF00547132

135. Oh HK, Son CH (2010) New correlation to predict the heat transfer coefficient in-tube

cooling of supercritical CO2 in horizontal macro-tubes. Exp Therm Fluid Sci 34:1230–

1241. https://doi.org/10.1016/j.expthermflusci.2010.05.002

136. Hoeschele M, Springer D, German A, et al (2015) Strategy Guideline: Proper Water

Heater Selection

APPENDIX. ADDITIONAL PARAMETRIC STUDY

Figure A1 shows the effect of ambient temperature on the heat pump COP (Figure A1a), compressor power consumption (Figure A1b), water heat absorption (Figure A1c), and outlet water temperature (Figure A1d) at the baseline operating conditions. The heat pump COP increases to its maximum value and then decreases with the ambient temperature (Figure A1a). The reason for this relationship is the competing effects of the higher work input and higher heat transfer with increasing ambient temperature. As the ambient temperature increases, the evaporator inlet quality decreases for a fixed evaporator outlet condition. As a result, the compressor discharge pressure increases, which causes the compressor power consumption to increase (Figure A1b). At the same time, the heat transfer to the water in the gas cooler also increases (Figure A1c) due to an increase in refrigerant temperature at the gas cooler inlet at higher discharge pressure. The heat pump COP increases until the CO_2 temperature at the gas cooler outlet reaches 23 °C. At gas cooler outlet temperatures below 23 °C, the resulting compressor power consumption is high enough to reduce the heat pump COP even though the water heat absorption increases. However, despite the changes in COP, the water outlet temperature increases monotonically with ambient temperature (Figure A1d) because the heat absorption continues to increase. For example, at the baseline conditions, the COP is 3.77 at an ambient temperature of 80 °C, increases to 4.27 at an ambient temperature of 20 °C then decreases to 4.03 at 24 °C. The corresponding water outlet temperature increases from 49 to 69 to 80 °C.
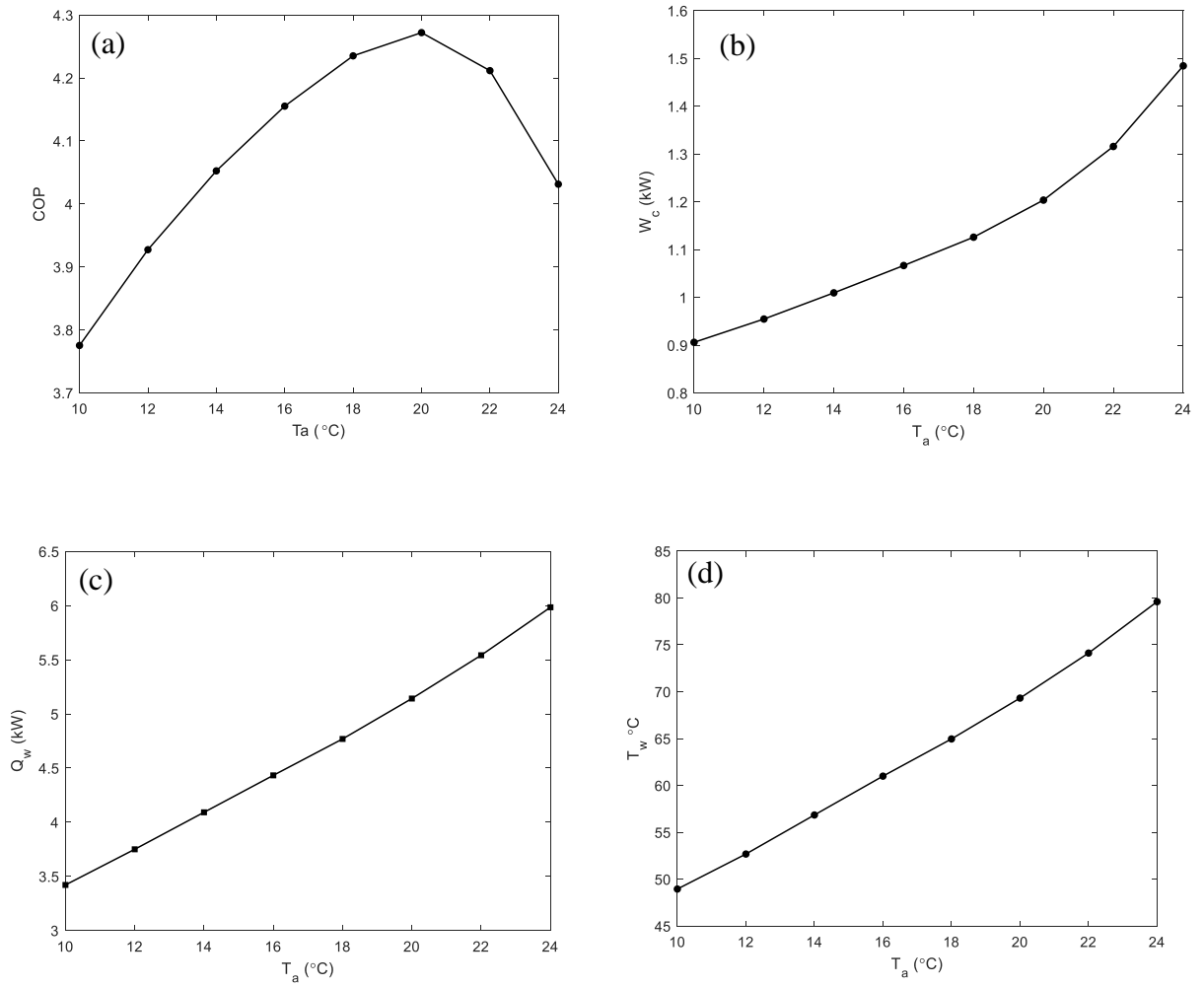
Figure A1: Effect of ambient temperature on the (a) heat pump COP, (b) compressor power consumption, (c) water heat absorption, (d) water outlet temperature at the baseline operating conditions.